The Dissertation Committee for Mark Edward Ferraro Certifies that this is the approved version of the following dissertation:

Graphoepitaxy for Directed Self-Assembly of Particle Monolayers

Committee:

Roger T. Bonnecaze, Co-Supervisor

Thomas M. Truskett, Co-Supervisor

Venkat Ganesan

Graeme Henkelman

Carlton Grant Willson

Graphoepitaxy for Directed Self-Assembly of Particle Monolayers

by

Mark Edward Ferraro, B.S.

Dissertation

Presented to the Faculty of the Graduate School of

The University of Texas at Austin

in Partial Fulfillment

of the Requirements

for the Degree of

Doctor of Philosophy

The University of Texas at Austin

May 2016

Dedicated to my parents

Acknowledgements

First and foremost, I would like to thank my advisors Roger Bonnecaze and Tom Truskett. Without the guidance and support from the two of you, none of this would be possible. I still remember our meetings during my first year of graduate school, when we were first formulating the project. Listening to you bounce ideas off each other could occasionally be intimidating, as I had yet to learn many of the concepts you were discussing. But I quickly began to understand more and more, and eventually reached a point where I felt I could confidently contribute to the conversation. I now realize how beneficial it was to hear you two describe your thought process on how to construct a research plan. This gave me insight into how successful researchers investigate a problem, and taught me how to ask the right questions. Thank you for your patience and support throughout the years. I couldn't ask for better advisors.

I would also like to extend my gratitude to Kris Wise and the NASA Space Technology Research Fellowship team. The NSTRF program has opened doors to a number of opportunities that I would not have had otherwise. Thank you Kris for your input on my progress reports, and I truly appreciate the time you took to host me during my visit to NASA Langley Research Center. I'd also like to thank Frank van Swol and Vince Shen for bringing me in to Sandia and NIST, and for their help with various portions of my project.

Thank you to the members of my thesis committee, Dr. Ganesan, Dr. Henkelman, and Dr. Willson. Your input truly helped guide the completion this project. Dr. Willson, I appreciate your help visualizing the future validation experiments for this work. And

Dr. Ganesan, thank you for being an excellent professor. Your courses were always challenging, but I was certainly able to learn a lot from them.

I'd also like to acknowledge the support from everyone in the Bonnecaze and Truskett research groups. Parag, Talha, Michael, and Shruti, thanks for being wonderful office mates. Avni, Lavanya, Akhilesh, Ben, Meghali, Andrew, Muhammed, James, Jon, Kyle, Stephanie, Soumik, Xilan, thank you for all of the great conversations, both work-related and otherwise. And thanks to Mark Pond for convincing me to come to UT-Austin during my graduate recruiting weekend.

I must also thank my longtime friends Dan and Raleigh. It's rare to find such kindred spirits so early in life, and I consider myself lucky to have grown up with the two of you. You both provided a constant source of motivation and support, and I wouldn't be where I am today without you. Dan, I am so grateful for our frequent conversations and for your help through stressful times over the last few years. Raleigh, I always looked forward to conferences we were able to attend together. It was far easier to give a presentation when you were in the audience.

Finally, I need to express my enormous gratitude to my parents. Your love and support means the world to me, and I wouldn't be the person I am today without your guidance. Thank you for always being there when I need you and for your support through difficult times. And thank you for being a constant example of the kind of person I want to be as I get older. You always put me in a position to succeed and to lead a happy, fulfilling life. Thank you for everything.

Graphoepitaxy for Directed Self-Assembly of Particle Monolayers

Mark Edward Ferraro, Ph.D.

The University of Texas at Austin, 2016

Co-Supervisors: Roger T. Bonnecaze and Thomas M. Truskett

Many promising nanotechnologies, such as bit-patterned magnetic media, require highly ordered, defect-free monolayers of particles. Thus, there is a need for cost-efficient and robust manufacturing techniques to reliably fabricate such structures. Self-assembly of particles from suspensions has emerged as a promising nanomanufacturing method, and the tunability of nanoparticle interactions can lead to a diverse array of thermodynamically accessible structures. Nonetheless, particles deposited on surfaces in the absence of external bias often form highly defective structures. Recently, template-directed self-assembly techniques such as graphoepitaxy have been successfully applied to produce low-defectivity block copolymer morphologies with desired nanoscale features. The role of a template in directing the assembly of particulate systems, however, is still poorly understood. The use of larger scale patterned substrates to drive smaller scale assembly of particle monolayers can potentially expand the set of achievable lattices, and could be used in nanopatterning processes or in the manufacture of functional materials.

In this dissertation, classical density functional theory (DFT), grand canonical Monte Carlo (GCMC) simulations, and cell theory are used to assess the suitability of graphoepitaxial assembly for particle monolayers and to predict the limits of pattern multiplication in three separate systems. The first two involve the assembly of hard

sphere and hard rectangle particle monolayers on surfaces with closed square and closed rectangle template geometries, respectively. The third involves the assembly of spherical and rectangular particles on surfaces patterned with posts. Pattern multiplication limits for these systems (~10x) can be understood in terms of the balance between favorable enthaplically-driven structuring near the boundaries and unfavorable loss of configurational entropy upon forming the targeted structure.

Table of Contents

List of Figures

Chapter 1: Introduction

1.1 MOTIVATION

High precision, low-cost fabrication of nanostructures with low defectivity is essential for the commercial production of nano-enabled devices. There are a growing number of applications that take advantage of nanometer-scale patterns. Such features can significantly enhance light absorption in plasmonic materials [1,2], bit patterned magnetic media can greatly increase the memory density on a hard drive [3,4], and nanostructured materials can considerably improve efficiency in fuel cells [5]. Furthermore, it is possible to control material properties through nanoscopic lattice structure, which can result in new classes of metamaterials with thermal and optic properties not seen in nature [6-10]. As we continue to discover more about the novel physics of nanoscale patterns, we lack adequate tools that enable the reliable, low-cost manufacture of materials required for many of these technologies. Currently, manufacture of nanopatterns relies heavily on top-down lithography techniques, such as photo-imprint lithography [11,12]. Despite their successes, one of the challenges facing such lithographic methods is their inability to generate patterns smaller than 20nm in a way that is reliable, cost-effective and rapid enough for industrial-scale manufacturing processes [13]. In order to achieve the requisite length scales for the aforementioned applications, it may be necessary to incorporate bottom-up nanomanufacturing techniques. Recent advances in nanoparticle design opens new avenues for the inclusion of self-assembly as an interesting (although still poorly understood) alternative approach to cheaply nanopattern and fabricate functional materials.

There are many examples that illustrate the possibilities of self-assembly, both in nature (DNA, protein folding, etc.) and through artificial means [14]. While nanoparticles have shown great promise in self-assembly [15-22], it is also widely appreciated that processes involving nanoparticles are limited in terms of the number of large-scale, low-defect structures that they can produce under various thermodynamic conditions. If self-assembly is to become a reliable nanomanufacturing tool, we must uncover new ways to fabricate a more diverse set of equilibrium structures in a cost-effective and defect-free manner. For example, bit-patterned magnetic media requires 2D square lattices with approximately 10nm material features (e.g., particles) placed with less than 5% deviation from desired lattice coordinates [23]. It is not clear if material systems that meet these specifications can be formed from self-assembly processes alone.

This is where "directed" self-assembly provides a unique opportunity. It is possible to expand the set of thermodynamically accessible lattices by exposing the assembling particles to an external field [24]. For example, in 2D self-assembly applications, the external field might be a chemically or topographically prepatterned surface that guides the assembly of deposited nanoparticles. The external field can act as a corrective force that limits defects in the self-assembled lattices. In fact recent developments have shown that highly detailed external fields can fix individual particles in desired locations [25,26]. However, in many cases, this would require an external field that is patterned at the same length-scale as the final assembled structure, thus negating the primary pattern multiplication benefit of self-assembly. The challenge for designing methods of directed self-assembly is to find the appropriate combination of particle interactions and external fields to minimize the requisite direction on the system. In other words, we can look to use traditional top-down techniques to create a pattern on a coarse

length-scale to direct the self-assembly of particles on a finer scale. Ultimately, we wish to know the extent of this pattern multiplication that can be induced by an external field.

The projects outlined in this dissertation seek to elucidate the possibilities and limitations of the directed self-assembly approach. Since there is still much to learn about the behavior of self-assembled particles in the presence of an external field, we will analyze various model particle/field systems to discover the limitations that direction can have on the lattice structure of particulate systems. As the external fields investigated in these projects will ultimately be fabricated through lithographic processes, the focus will be on 2D structures formed by particles in suspension adsorbing to a prepatterned substrate. Specifically, the goal of this project is to create computational tools that help discover new directed self-assembly strategies for scalable nanomanufacturing.

1.2 SELF-ASSEMBLY

The term "self-assembly" is broad in scope, as it covers a wide variety of techniques that can lead to the spontaneous formation of materials with nanometer scale structures. The challenge for applying self-assembly to nanomanufacturing applications is to select an appropriate system of tunable interaction parameters that can be experimentally adjusted to produce a desired structure with acceptable level of defects. Nanoparticles are interesting for self-assembly because their interactions can be systematically modified, allowing them to assemble into different periodic patterns with length scales that are not easily imposed via top-down fabrication approaches. Because of this, nanoparticle self-assembly has become an active research field in recent years. Existing literature on the subject provides many ways of manipulating interparticle interactions and documents the accessible structures observed for each [27-32].

However, there are still gaps that need to be filled before self-assembly can be broadly applied to any nanomanufacturing process. Currently, most self-assembled structures are relatively simple lattices seen in nature. More complicated structures can be achieved, but require very intricate particle designs that would be difficult and expensive to fabricate.

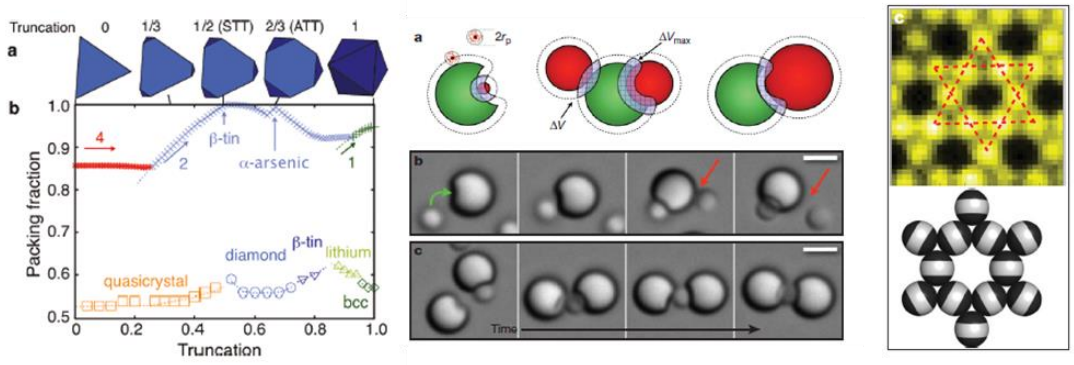

Figure 1.1: Currently, there are a number of ways to design interparticle interactions for self-assembly. For example, it is possible to adjust particle shape to influence local packing (left), design concave particle features to utilize solvent depletion interactions (middle), and it is possible to use triblock Janus particles (right) with hydrophobic caps which cluster together, forming a kagome lattice. While these interactions are able to form novel structures, their complexity makes it difficult for the precise mass production required for nanofabrication process. Figures from left to right appear in Damasceno et al., ACS Nano (2012) [33], Sacanna et al., Nature (2010) [19], and Chen et al., Nature (2011) [17].

In order to mitigate some of the aforementioned manufacturing concerns, one can envision applying an external field to a system of nanoparticles in an attempt to achieve more complicated lattices without requiring particles that are so difficult to manufacture. If an external field can apply a small energetic penalty to competing lattices, it could potentially expand the range over which a desired lattice is stable, allowing for more tolerance for defective structure.

1.3 GRAPHOEPITAXY FOR DIRECTED SELF-ASSEMBLY

Field directed assembly has been extensively explored for the assembly of block copolymers (BCPs) [34-44]. Block copolymer systems undergo various types of phase transitions depending on parameters such as block chain length, interfacial interactions, and thickness of BCP thin films [45-52]. Assembled structures can consist of lamellae, spheres, gyroids, and cylinders with dimensions as small as 5nm [53-61]. It is further possible to carefully design a surface template of features with affinity to one of the blocks can control the locations of these phase boundaries. Additionally, one may control the equilibrium pattern simply by confining the polymer with topographical template features [34,62-64]. This method of graphoepitaxy has shown it can effectively induce pattern multiplication in block copolymer systems, generating details many times smaller than that of the prepatterned template [65]. However, these methods take advantage of the structure and binding capabilities of the polymers, and need modification before application to nanoparticle systems. As particulate systems do not exhibit the same phase separation as polymeric materials, it is an open question as to how far the effect of a template feature can propagate through the self-assembled structure of a particle system.

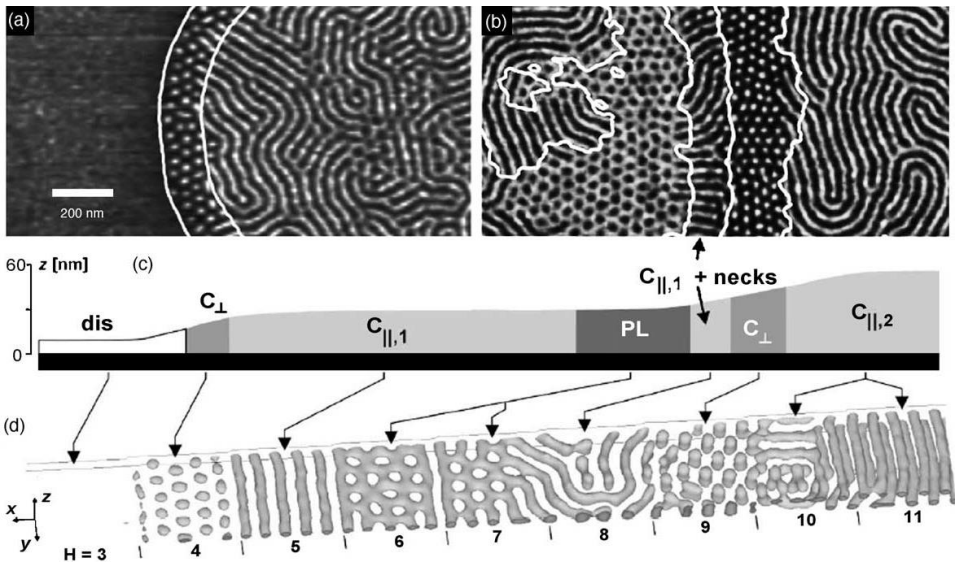

Figure 1.2: Commensurability of the film thickness greatly influences phase behavior of block copolymers. Images (a) and (b) show phase behavior of poly(styrene-*block*-butadiene-*block*-styrene) triblock copolymers for a thickness profile in (c). Part (d) illustrates simulation results of the same copolymer system. This dependence on commensurate thickness can potentially be exploited through graphoepitaxial assembly. Figure appears in Segalman, Mater. Sci. Eng. (2005) [66]

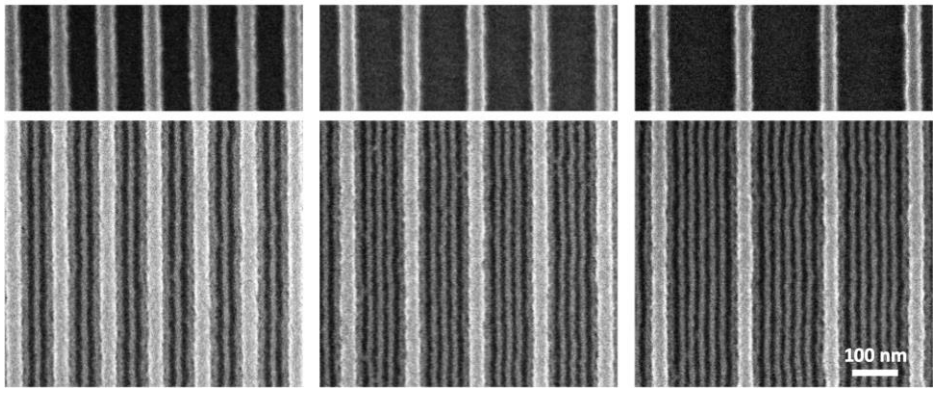

Figure 1.3: Graphoepitaxy of lamella-forming poly(styrene-*block*-trimethylsilylstyrene) (PS−PTMSS). Polymers assemble in etched topographical trenches of a width commensurate to lamellar periodicity. SEM micrographs above show that density multiplication was successful 3x (left), 5x (middle), and 7x (right) trench subdivisions. Figure appears in Maher et al., Appl. Mater. Interfaces (2015) [65].

Knowledge of block copolymer behavior can be of great benefit to directed assembly of particulate systems. While there has been limited work in the latter area, the study of particles directed by a field remains open with many unanswered questions, despite a number of advantages unique to particle deposition. Particles can be solution processed [67], easily manufactured with reliable precision [68,69], and can allow for the direct patterning of functional materials [70,71]. Similar to the copolymers, we already know that with enough of a framework, nanoparticles can be forced into desired locations [72,73], but there are still many open optimization questions. A greater understanding of particle directed self-assembly can open new avenues to fabrication of novel, useful nanodevices.

In the following chapters, this dissertation will investigate the minimum amount of existing scaffolding required to allow nanoparticles to build the desired defect-free pattern (i.e., how much direction is required for directed self-assembly). Through use of various computational tools I intend to show that it is possible to use a prepatterned substrate to direct the assembly of particle monolayers, even for pairwise interactions lacking any enthalpic component. The desired impact is to design a set of templates to guide particle assembly for nanomanufacturing applications. Surprisingly, this area lacks a universally accepted set of production strategies. As a result, any advances that allow for reliable, cost-efficient manufacturing strategies could have a profound effect on the fields of nanotechnology and material science.

This dissertation will primarily explore three separate systems. Chapter 2 will begin by analyzing assembly of hard sphere monolayers in confined template geometries. As these particles exhibit such simplistic pairwise interactions, a study of their assembly can provide valuable insight into the fundamental forces affecting self-assembly. Chapter 3 will continue this work by introducing particle anisotropy. This inclusion introduces

two opposing phenomena: configurational entropy of rotating anisotropic particles and directional interactions propagating template effects. This chapter will explore the limiting density multiplication before configurational entropy becomes the dominant driver of assembly. Where preceding chapters focus on fully confined templates, Chapter 4 will explore the ability of open template structures (e.g. truncate walls, fixed particle posts) to generate similar order to closed templates. Finally, Chapter 5 will provide a cell theory scaling argument to further explore the physical constraints on pattern multiplication. Suggestions for future directions will be outlined in Chapter 6.

Chapter 2: Graphoepitaxy of Spherical Particle Monolayers

2.1 INTRODUCTION

Current work in particle self-assembly focuses on complicated interparticle interactions, and the particles that exhibit those interactions can be difficult to fabricate with the precision necessary for nanomanufacturing purposes. To remedy this, we begin our analysis through particles with perhaps the simplest pairwise interaction: hard spheres. A study of hard sphere assembly essentially becomes an investigation of optimal packing, and consequently, the entropic forces driving lattice formation. Thus, the primary question is whether a template can provide sufficient confinement to entropically favor a target structure as an optimal packing.

In this chapter we consider a model for the solution-based deposition and assembly of spherical particles onto a smooth, attractive surface with regularly spaced enthalpic barriers that represent, for example, prepatterned chemical or topographical features. Particles from a contacting fluid suspension can adsorb onto or desorb from the substrate, where they diffuse in the presence of the periodic barriers. As the liquid film dries, the equilibrium surface concentration increases until only a monolayer of deposited particles remains. For hard-sphere particles on a pattern-free substrate, a disordered liquid-like structure is favored for areal packing fractions $\eta < 0.72$. Above $\eta = 0.72$, a hexagonally close-packed (hcp) solid forms [74]. To successfully direct the particles into an alternative packing at high η, an appropriately designed external field provided by the substrate must

---

This work has previously appeared in M.E. Ferraro, R.T. Bonnecaze, and T.M. Truskett, "Graphoepitaxy for Pattern Multiplication of Nanoparticle Monolayers," *Phys. Rev. Lett*. **113**, 085503 (2014) [92]. Mark Ferraro carried out the Monte Carlo simulations and density functional theory calculations, and contributed to the data analysis.

favor the targeted structure over the otherwise entropically favored hcp lattice. This type of graphoepitaxial assembly has been successfully used in other contexts, e.g., to direct the assembly of block copolymer films into targeted morphologies [35-44].

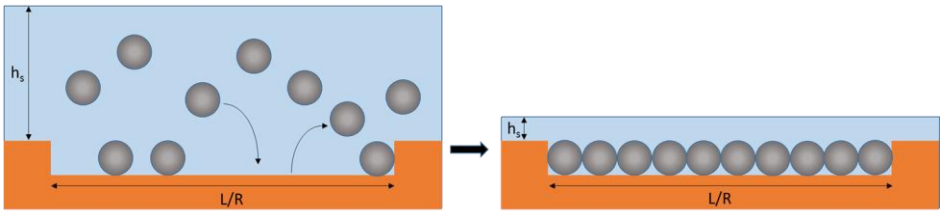

Figure 2.1: An illustration of the hard sphere deposition process. Particles in suspension are free to adsorb to a prepatterned substrate. As the solvent evaporates, chemical potential in the suspension increases, driving more particles to the surface. When exposed to the template, which may consist of a topographical (illustrated here) or chemical features separated by some distance L, particles are directed toward assembly of a target structure.

We study a model for such an elementary pattern multiplication process for deposited particulate films. We show that a smooth substrate with a periodic square pattern of enthalpic barriers is able to generally disrupt formation of the hcp lattice in favor of a square lattice structure as the surface concentration increases. Interestingly, this approach remains effective even when the barriers are separated by length scales significantly (~10x) larger than the particle diameter (i.e., the lattice constant), illustrating the promise of using graphoepitaxy for directing particulate assemblies of patterned monolayers.

2.2 Simulation Methods

Rosenfeld's Fundamental Measure Theory (FMT) [75] provides accurate equilibrium density profiles for inhomogeneous hard-particle fluids with greater computational efficiency than Monte Carlo simulations [76]. The FMT framework is also ideal for answering inverse design questions for targeted self-assembly, which—while not addressed specifically here—is a fruitful area for future study. We adopt a version of FMT

recently introduced by Roth et al. [77] which faithfully reproduces the structure of high-density fluid states as well as the first-order fluid-to-hcp phase transition. Density functional theory methods are useful in that they can provide an approximation for excess Helmholtz free energy, F_{ex}, for a given pairwise interaction $V_{ij}(r)$ and the corresponding Mayer-f function $f = \exp(-\beta V_{ij}(r))$. Rosenfeld's unique contribution for this density functional theory is the decomposition of the Mayer-f function into convolution products of geometric weighting functions. This deconvolution is exact in 1 or 3 dimensions, but in even dimensions requires an infinite series of scalar (ω_α) and tensor ($\omega^{(m)}$) weighting functions. The two dimensional expansion used by Roth et al. truncates beyond the second order tensor term, resulting in the following weight functions:

$$\omega_0(\mathbf{r}) = \frac{1}{2\pi R}\delta(R - |\mathbf{r}|), \quad (1)$$

$$\omega_2(\mathbf{r}) = \Theta(R - |\mathbf{r}|), \quad (2)$$

$$\omega^{(0)}(\boldsymbol{r}) = \delta(R - |\mathbf{r}|), \quad (3)$$

$$\omega^{(1)}(\boldsymbol{r}) = \mathbf{r}\,\delta(R - |\mathbf{r}|), \quad (4)$$

$$\omega^{(2)}(\boldsymbol{r}) = \mathbf{r}\,\mathbf{r}\,\delta(R - |\mathbf{r}|), \quad (5)$$

where δ is the Dirac delta and Θ is the Heaviside step function. Convolution integrals of these weight functions with the density profile introduces scalar and tensoral weighted densities defined as

$$n_\alpha = \int d\mathbf{r}'\rho(\mathbf{r}')\omega_\alpha(\mathbf{r} - \mathbf{r}'), \quad (6)$$

$$n^{(m)} = \int d\mathbf{r}'\rho(\mathbf{r}')n^{(m)}(\mathbf{r} - \mathbf{r}'). \quad (7)$$

These weighted density functions allow for an ansatz of the excess free energy density $\beta F_{ex}[\rho] = \int d\mathbf{r}\Phi(\mathbf{r})$ where dimensional analysis and the Scaled Particle Theory equation of state provide an assumed form:

$$\Phi = -n_0 \ln(1 - n_2) + \frac{1}{4\pi(1 - n_2)} \sum_{m=0}^{\infty} C_m n^{(m)} \cdot n^{(m)} \quad (9)$$

As noted, the infinite series in the above expression is truncated beyond second order tensors, resulting in three unknown coefficients C_0, C_1, and C_2. Further constraints from the second virial coefficient and the 0D limit reduce the approximation of these coefficients to a single variable which can be obtained through a least squares fit to the Mayer-f function. This provides the expression,

$$\Phi(\{n_\alpha, n^{(m)}\}) = -n_0 \ln(1-n_2) + \frac{1}{4\pi(1-n_2)}\left(\frac{19}{12}\left(n^{(0)}\right)^2 - \frac{5}{12}n^{(1)}\cdot n^{(1)} - \frac{7}{6}n^{(2)}:n^{(2)}\right) \qquad (10)$$

This can then be used to represent the excess Helmholtz free energy, and thus the grand canonical free energy,

$$\beta\Omega[\rho] = \int d\mathbf{r}[\Phi[\rho] + \rho(\mathbf{r})(\ln\rho(\mathbf{r}) - 1 - \beta\mu)]. \qquad (11)$$

The equilibrium density profile may then be found through minimization via the functional derivative $\frac{\delta\Omega}{\delta\rho} = 0$.

For computational efficiency, equilibrium FMT computations reported here use a matrix-free Newton iterative method developed by Sears and Frink [78]. For our 2D GCMC simulations of the same model system, we adopted a simulated tempering algorithm designed to study high-density hard-particle systems in the vicinity of the melting transition [79].

2.3 MODEL SYSTEM

In our model 3D hard spheres—once adsorbed on the 2D substrate—interact with each other as exclusion disks in the grand canonical ensemble with an external field (representing the prepatterned barriers) and with a chemical potential set by the reservoir of particles in the contacting fluid suspension. Slow evaporation of the solvent concentrates the reservoir, thus raising the chemical potential and increasing the particle concentration on the surface. Increasing the particle-substrate attraction at constant reservoir concentration would

have the same net effect. We model the thermodynamics and structure of the adsorbed monolayer as a function of chemical potential and template features (i.e., barrier height and separation) using classical density functional theory and Grand Canonical Monte Carlo (GCMC) simulations.

For our target structure, we choose a periodic square lattice, which is of interest for bit-patterned magnetic media [80]. The square lattice has a lower coordination number (4 vs. 6) and a less efficient packing structure than the hcp crystal, which means that, for hard spheres, graphoepitaxy will be required to make it the thermodynamically stable structure. The trivial graphoepitaxial solution would be to use substrates with parallel barriers that intersect to form adjacent square "boxes" with side lengths equal to twice the particle radius, $2R$, so that—once adsorbed—each particle is precisely confined to its desired lattice position (Figure 2.2(a)). This, of course, in addition to having other practical limitations, requires accurate pre-patterning on the same length scale as the target lattice, which negates the most powerful pattern amplification benefits of directed self-assembly. Thus, we consider here square templates of barriers separated by integer multiples of the particle diameter; that is, sparser patterns commensurate with the desired square lattice periodicity (Figure 2.2(b)). The barriers are energy step functions of width 2R and normalized "height" βV_{ext} ($\beta=1/k_B T$, where k_B is the Boltzmann constant and T is temperature) acting on particle centers; i.e., they penalize any "overlap" of a particle with the infinitely thin line defining the square template boundary. This template allows us to direct assembly of particles into periodic, close-packed square-lattice structures. For generality, we present results in terms of the normalized chemical potential $\beta(\mu-\mu_{hcp})$ where $\beta\mu_{hcp}$ is the chemical potential for which the 2D hcp solid becomes the thermodynamically stable adsorbed phase on a patternless substrate.

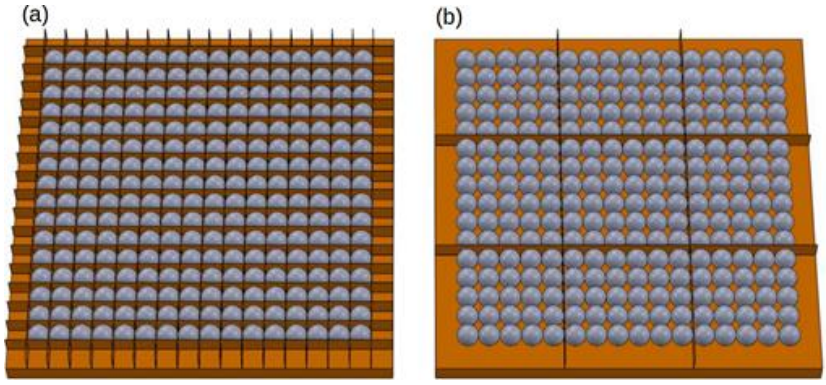

Figure 2.2: Monolayers assembled via deposition onto a substrate with thin repulsive barrier templates separated by a distance commensurate with the square lattice unit cell. The template in (a) trivially fixes each particle in its ideal location. The template in (b) uses sparser templating to direct assembly into the same structure.

2.4 RESULTS AND DISCUSSION

2.4.1 FMT Predictions for a Square Template

Figure 2.3 shows the equilibrium density profiles predicted by FMT as a function of increasing barrier height of the template. In this figure the chemical potential ($\beta(\mu-\mu_{hcp}) = 2.40$) is higher than what would be otherwise necessary to form the hcp structure with a pattern-free substrate (see Figure 2.3(a)). When particles absorb in the presence of the template, the equilibrium density profile qualitatively changes and is characterized by structures with square symmetry (Figures 2.3(b),(c)), even for a barrier height as low as $\beta V_{ext,}= 2$. For increasing values of barrier height, the density profiles become sharper and the square lattice structure more pronounced. It is interesting to note that the template feature separation in Figure 2.3 is nearly commensurate for both the hcp and square lattices, and yet the square symmetry is still clearly preferred in the presence of finite barriers.

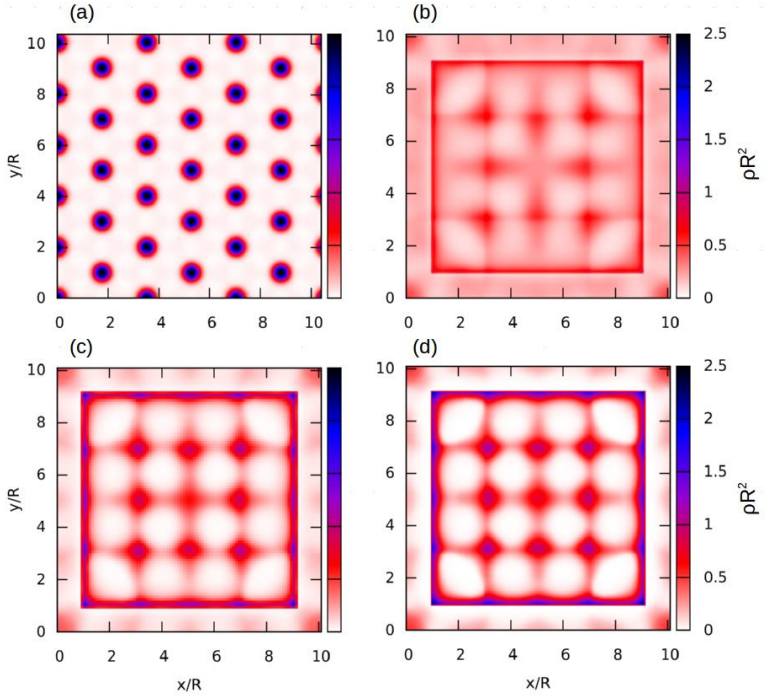

Figure 2.3: Equilibrium density profiles with $\beta(\mu-\mu_{hcp}) = 2.40$ predicted using FMT. The external field is as illustrated in Figure 2.2(b), with barriers of height βV_{ext} = (a) 0, (b) 2, (c) 5, and (d) 10, each separated by a distance of 10R.

The effect of template spacing from 8R to 28R for βV_{ext},= 10 and $\beta(\mu-\mu_{hcp}) = 2.40$ is shown in Figure 2.4. Note that while the structuring weakens as the template spacing grows, the square symmetric order persists even when the spacing is an order of magnitude larger than the particle diameter. However, for template feature separations greater than 20R, the density peaks lower and spread and local maxima are not significantly greater than the bulk density. At a template spacing of 24R the density signature of a square pattern in the center has practically vanished, which indicates the barriers are too far apart to promote long range ordering (see also Figure 2.8 for Monte Carlo snapshots). As the wall separation increases to 28R, the density profile in the middle of the system is nearly flat.

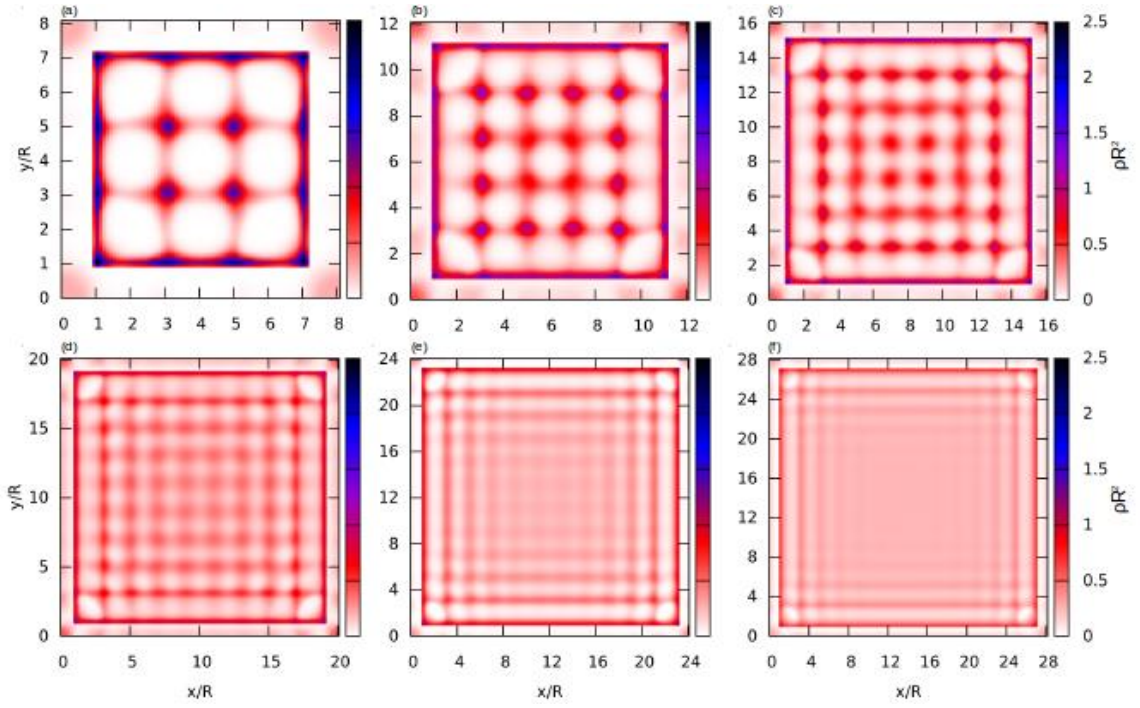

Figure 2.4: Equilibrium density profiles predicted by FMT as a function of template feature spacing for $\beta(\mu-\mu_{hcp}) = 2.40$. Enthalpic barriers of height $\beta V_{ext} = 10$ are placed at each border of the displayed region. Template feature separation for each profile is (a) 8R, (b) 12R, (c) 16R, (d) 20R, (e) 24R, and (f) 28R.

2.4.2 GCMC Study of the Effect of Chemical Potential on Assembly

While the FMT density profiles provide useful average information about the structural consequences of the template features, we turn to grand canonical Monte Carlo (GCMC) simulations to characterize the defect statistics from the underlying microstates and understand how they evolve with increasing chemical potential and surface concentration. The occupancy probabilities for a 10Rx10R square obtained from GCMC simulations of a periodically-replicated 9-square system is shown in Figure 2.5. For normalized chemical potentials of $\beta(\mu-\mu_{hcp}) = 1.87$, some of the square regions in the template are perfectly filled and others are missing one or more particles (Figure 2.5b).

Perfectly filled regions form square lattices. Regions with one or two missing particle form structures with point defects and those with two or three missing particles resemble 2D liquid-like structures. Furthermore, these defective structures explain the qualitative features observed in the FMT density profiles. These profiles are obtained in the grand canonical ensemble, meaning they comprise microstates with different numbers of particles. Microstates with vacancies allow rows and columns to freely translate, which contributes to the average density on the grid connecting square lattice coordinates. As $\beta\mu$ increases, the fraction of microstates containing the ideal 25 particles smoothly increases. Virtually zero defectivity is achieved for $\beta(\mu-\mu_{hcp}) = 5.87$ and $\beta V_{ext} = 10$ with the structural configuration shown in Figure 2.5(c).

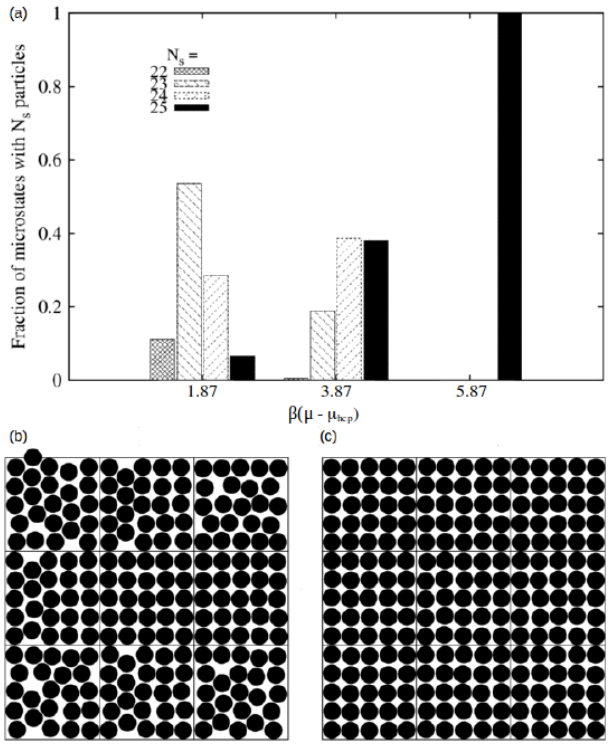

Figure 2.5: (a) Fraction of microstates with Ns particles as a function of chemical potential β(μ-μhcp). Here, a microstate is defined by a single periodic 10Rx10R square bounded by the external field from Figure 2.3(d). Configurations shown in (b) and (c) are snapshots taken from the GCMC simulations where β(μ-μhcp) = 1.87 and 5.87, respectively. Lines in plots (b) and (c) represent thin barriers of height βVext = 10.

The manner in which the defects in the square lattice naturally fill in as a function of chemical potential can be understood from a basic statistical mechanical argument. For inhomogeneous hard-disk systems, it can be shown that the position-dependent insertion probability is given by $P_{ins}(x,y) = \rho(x,y)\lambda^2/\exp(\beta\mu)$ [81] where λ is the thermal de Broglie wavelength. The probability of successfully inserting a particle is proportional to the equilibrium number density ρ(x,y) at that location. From the FMT density profiles in Figures 2.3 and 2.4, we see that graphoepitaxy naturally places peaks in the density profile at the preferred square lattice sites. Thus, particles preferentially adsorb at point defects in

the square lattice. As solvent evaporation occurs, the increasing chemical potential pushes more particles into these open lattice sites, driving the system toward a defect-free square lattice structure as shown in Figure 2.5(c).

2.4.3 Fractional Expansion of Template Spacing

Discussion to this point has focused on templates composed of four perpendicular, thin walls separated by a distance commensurate with the square lattice. However, it is interesting to note that the wall separation need not be an exact integer multiple of the square lattice periodicity (i.e., the particle diameter). The imposed field may be expanded by fractions of a particle radius, and still preserve square order. This is not entirely surprising, as for many lattices, there is a required expansion before a new particle can physically fit within the system. In addition to physically having room for a new particle, it must be thermodynamically favorable to restructure into a more tightly packed lattice. As illustrated in Figure 2.6 we have found that template walls may be spaced at a commensurate length plus an additional ~0.5R in order to preserve the square lattice.

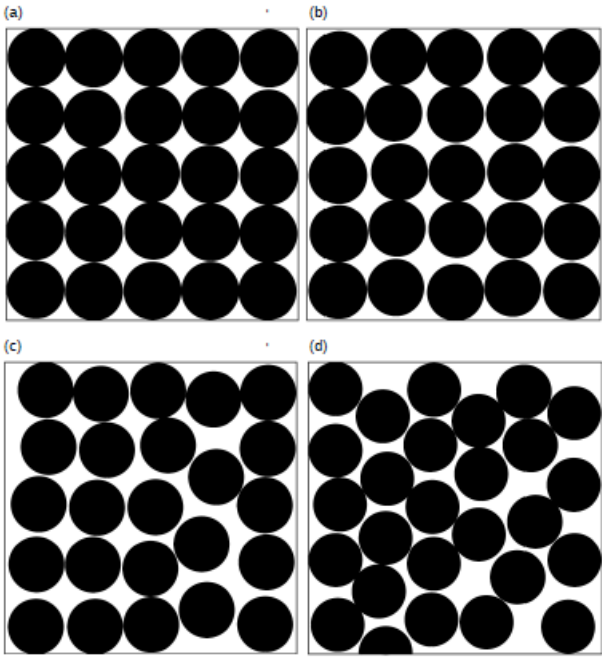

Figure 2.6: Hard sphere monolayers at $\beta(\mu-\mu_{hcp}) = 5.87$ exposed to an external field $\beta V_{ext} = 10$ with varying wall spacing. Distance between walls is (a) 10.2R, (b) 10.4R, (c) 10.6R, and (d) 11.0R where R is the particle radius.

2.4.4 Transition Away from Square Order

In Figure 2.4 we showed that peaks in the density profile for wall spacings beyond 20R (corresponding to a 10x10 lattice) are no longer well-defined. Analysis of this transition can be further supplemented by extracting a correlation length from the density profiles. This can be obtained by analyzing the decay in the height of local maxima for peaks further away from the template features. To quantify this decay, we introduce a new quantity, x_c, defined as the location where the peak height decays by a factor of 1/e. For sufficiently high order, x_c should be large, signifying that the height of each peak is not decaying quickly far from the wall. Low values of x_c indicate that wall effects decay rapidly as the system approaches the bulk density within a few particle diameters of the template feature.

We then observe a cross-section of the density profile taken from a middle row of the system (e.g., $\rho\left(\frac{x}{R}, \frac{L}{2R}\right)$) where wall effects are at their weakest. Density maxima from this cross-section are then normalized between 0 and 1 using $\bar{\rho} = \left(\rho(x/R) - \rho_{avg}\right)/\left(\rho(1) - \rho_{avg}\right)$, where $\rho(1)$ is the density against the wall. A value of $\bar{\rho}$ = 1 represents the maximum density in a given cross section, while $\bar{\rho}$ = 0 means the local density has reached the bulk density and localized order is no longer apparent.

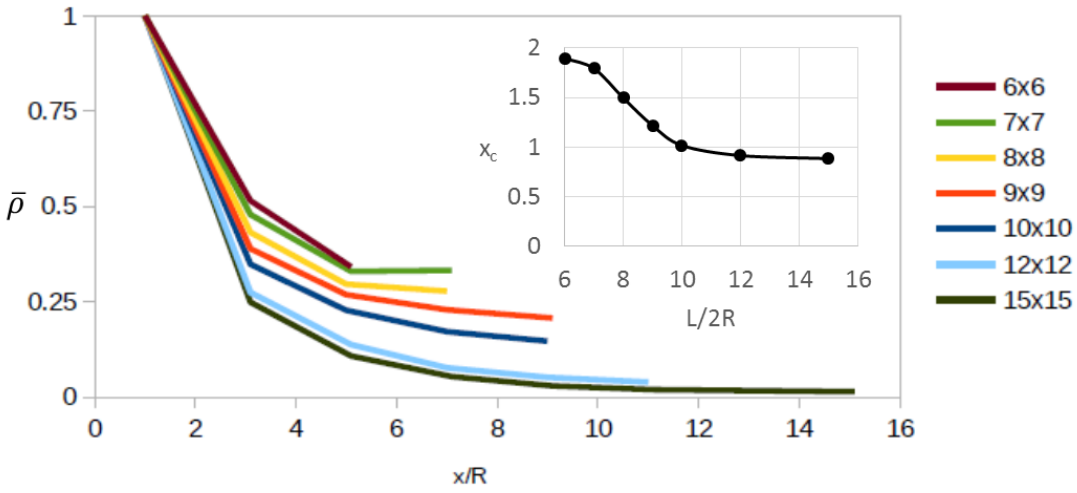

Figure 2.7: Local maxima of the middle cross-section ρ(x/R,L/2R) of density profiles for various wall-separations. Here, the density is normalized $\bar{\rho} = \left(\rho(x/R) - \rho_{avg}\right)/\left(\rho(1) - \rho_{avg}\right)$and x_c is defined as the value of (x-1)/2R where $\rho(x) = 1/e$. The height of the local maxima decreases quickly, with x_c occurring before the second peak for lattices greater than 10x10.

The value of x_c decreases dramatically, approaching the first non-contact peak in the profile by the 10x10 lattice. This pronounced decline in the propagation of wall effects further explains why the transition away from square order occurs around the 20R wall separation and, thus, why the corresponding sparser profiles in Figure 2.4 have such ill-defined peaks. This result is further clarified by grand canonical Monte Carlo simulations,

shown in Figure 2.8, which show a clear difference between the structures formed under the 20R and 24R wall separations.

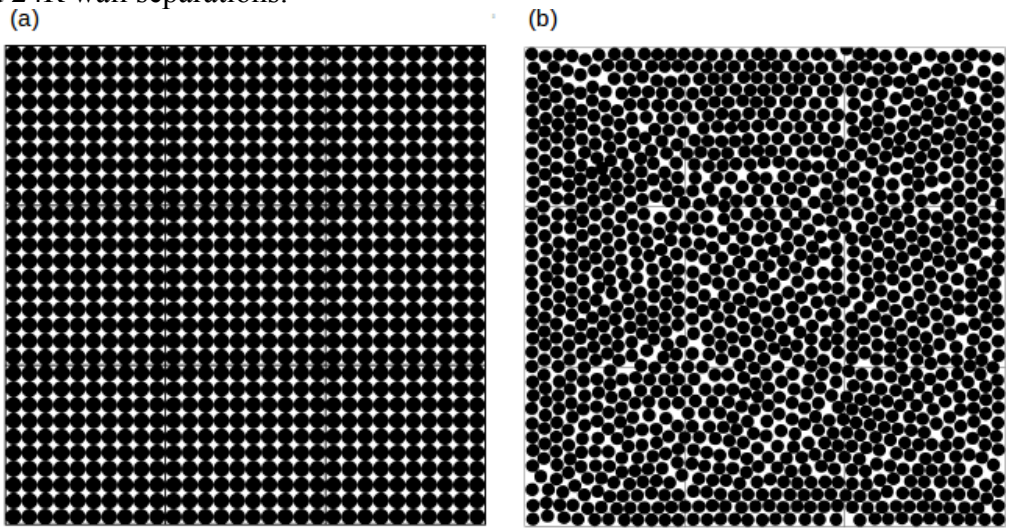

Figure 2.8: Grand canonical Monte Carlo snapshots of hard sphere monolayers at $\beta(\mu-\mu_{hcp}) = 5.87$ exposed to perpendicular walls of height $\beta V_{ext} = 10$ separated by (a) 20R and (b) 24R.

2.4.5 The Direct Pattern

While our work here has primarily focused on the effects of a sparse template, it is useful to see how a direct template behaves under similar conditions. As shown in Figure 2.9, a direct template is able to facilitate the formation of a square template at a lower chemical potential than the sparse templates (keeping in mind that direct patterning negates the pratical "pattern multiplication" benefits of a sparse template). This effect is due to the template fixing each particle in the ideal square lattice coordinate, even at low density. Thus, it becomes easier for each subsequent particle to enter in the desired location, as the existing particles do not require any restructuring. However, as chemical potential increases, the lattice for the direct template is very similar to that of the sparse template shown in Figure

2.5(c), though the complete square lattice is achieved at lower chemical potential in the direct pattern. This is likely due to the isolation of confined "cell." The probability of filling a given cell in the direct pattern is solely dependent on insertion energy, while the sparse template requires both insertion and structural rearrangement with will incur some energetic cost.

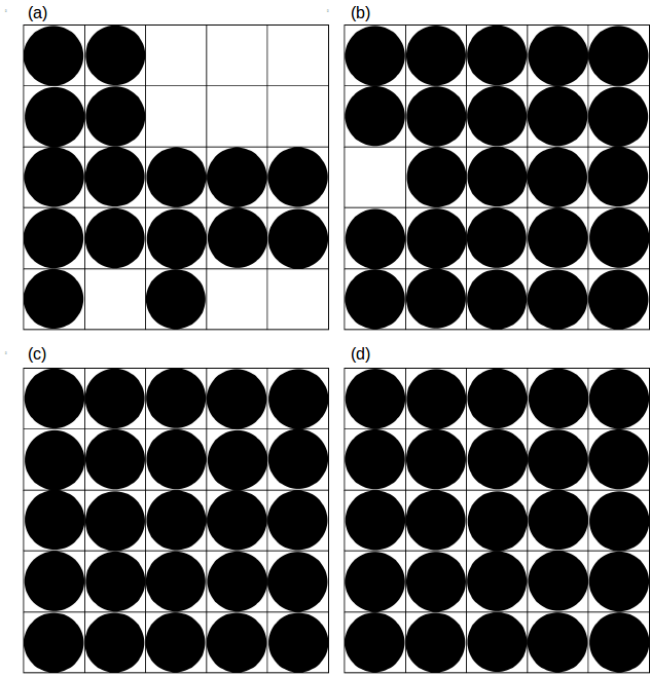

Figure 2.9: Grand canonical Monte Carlo snapshots of particles exposed to a direct pattern, with perpendicular walls spaced by 2R. Particle deposition is governed by chemical potential, $\beta(\mu-\mu hcp)$ = (a) -8.1, (b) -4.1, (c) 0.0, and (d) 3.9. As chemical potential increases, vacant wells are filled.

2.5 CONCLUSIONS

By focusing on athermal particles, the model system introduced here demonstrates how a substrate prepatterned with sparse, enthalpic template features can disrupt the otherwise entropically favorable packing of the hcp lattice in favor of a periodic structure

with square symmetry. It would be interesting to use FMT as a tool of inverse design to discover which template features and geometries would be optimal—within constraints specified by, e.g., a particular substrate preparation method—for obtaining not only square structures but other open 2D lattice packings of interest (kagome, honeycomb, snub square, etc.).

Moreover, to design a directed assembly process for specific material systems of technological interest, other interparticle interactions would also need to be considered. Such interactions might also be tuned, guided by theoretical methods similar to those discussed in [82-85], to complement the template's role in directing assembly into specific structures. For example, soft repulsive interparticle interactions have been shown to significantly reduce the thermodynamic favorability of the hcp packing over other open target structures of interest even on a pattern-free substrate [86].

Chapter 3: Translational and Orientational Order in Rectangular Particle Monolayers

3.1 INTRODUCTION

Work in the previous chapter has shown that the entropically favored two-dimensional (2D) hexagonal crystal favored by a monolayer of adsorbed hard-sphere particles on a smooth, substrate can be disrupted in favor of a square lattice structure by parallel, enthalpic barriers separated from each other by up to ten particle diameters. Here we evaluate whether similar graphoepitaxial barriers or templates can direct adsorbed rectangular particles into translationally and orientationally ordered rectangular monolayers. The choice of rectangular particles and the geometry of the array are motivated by the desired structures for bit-patterned magnetic media, where rectangular particles with aspect ratios around 2.3 have been shown to have the highest areal density that achieve desired read and write metrics [87].

Monolayers of hard-rectangular particles exhibit tetratic order illustrated in Figure 3.1(a) at an areal packing fraction $\eta > 0.7$ [88,89] in the absence of an external field. In the extreme limit placing a repulsive barrier around *each* particle would perfectly template its position and orientation, but negates any benefits of pattern multiplication by the self-assembly process. Here we study using Grand Canonical Monte Carlo (GCMC) simulations and density functional theory (DFT) predictions nontrivial pattern multiplication effects, considering wall separations of approximately $L_y/R = n$ *and* $L_x/R =$

This work has previously appeared in M.E. Ferraro, T.M. Truskett, and R.T. Bonnecaze, "Graphoepitaxy for Translational and Orientational Ordering of Monolayers of Rectangular Particles," *Phys. Rev. E* **93**, 032606 (2016) [102]. Mark Ferraro carried out the Monte Carlo simulations and density functional theory calculations, and contributed to the data analysis.

an, for integer values of $n>1$. These patterns are represented as enthalpic barriers, separated by lengths L_x and L_y in the *x*- and *y*-directions, respectively. The dimensions of the rectangular particles are R and aR, where $a > 1$ is the particle aspect ratio. Additionally, while the inclusion of particle anisotropy introduces the importance of wall separation in two directions, we focus here on practically interesting template boundaries with aspect ratios near unity as illustrated for example in Figure 1(b).

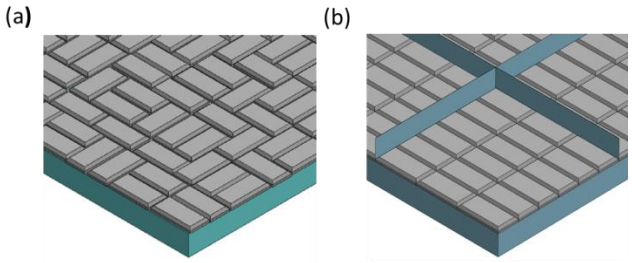

Figure 3.1: Rectangular particle monolayer assemblies (a) exhibiting tetratic order with no template pattern, and (b) ordered into the desired rectangular lattice by thin, topographical barriers.

3.2 Simulation Methods

3.2.1 Grand Canonical Monte Carlo

Due to the near close packed surface coverage of rectangular particles realized at high chemical potentials (e.g., high concentration due to evaporation of the solvent), we utilize a growth-expanded ensemble for computational efficiency in our grand canonical Monte Carlo (GCMC) simulations [90]. This allows particles to enter the system at 20% of their true size, subsequently growing over the course of the simulation. Monte Carlo steps include arbitrary translation, rotation, insertion, deletion, or growth of a single particle. Only microstates comprising fully grown particles are considered in the equilibrium statistics. Periodic boundary conditions are imposed and simulations are conducted for various initial conditions.

3.2.2 Fundamental Measure Theory

As a supplement to the Grand Canonical Monte Carlo simulations, we again used Fundamental Measure Theory to investigate energy minimizing structures in the presence of rectangular templates. Due to the geometric nature of the deconvolution of the Mayer-f function, it is possible to modify the previous weight functions to model rectangular particles. While no FMT has been developed for freely rotating rectangular particles, it is possible to approximate this system through a bidisperse mixture of vertically and horizontally aligned particles [91]. This model utilizes the typical Helmholtz free energy functional $F[\rho_i]$ expressed as the sum of the ideal $F_{id}[\rho_i]$ and excess $F_{ex}[\rho_i]$ components. The ideal free energy assumes the usual functional

$$\beta F_{id}[\rho_i] = \sum_i \int_A dr \rho_i(r)\{\ln[\rho_i(r)\lambda_i^3] - 1\}, \quad (1)$$

where $\beta = 1/k_B T$ and λ_i is the thermal wavelength. As with all FMT models, the excess component is expressed as

$$\beta F_{ex}[\rho_i] = \int_A d\boldsymbol{r}\Phi(\boldsymbol{r}) \quad (2)$$

$$\text{where,} \quad \Phi = -n_0(\boldsymbol{r})\ln[1 - n_2(\boldsymbol{r})] + \frac{n_{1x}(\boldsymbol{r})n_{1y}(\boldsymbol{r})}{1 - n_2(\boldsymbol{r})} \quad (3)$$

Equation (3) represents is a local free energy density composed of weighted density functions, $n_\alpha(\boldsymbol{r})$. These weighted density functions are convolution integrals of the local density with geometric weighting functions, $\omega_i^{(\alpha)}(\boldsymbol{r})$, which represent geometric measures of the particles. For rectangles, the following weighting functions correspond to corners, edge lengths and surface area:

$$\omega_i^{(0)}(\boldsymbol{r}) = \frac{1}{4}\delta\left(\frac{\sigma_x^i}{2} - |x|\right)\delta\left(\frac{\sigma_y^i}{2} - |y|\right), \quad (4)$$

$$\omega_i^{(1x)}(\boldsymbol{r}) = \frac{1}{2}\Theta\left(\frac{\sigma_x^i}{2} - |x|\right)\delta\left(\frac{\sigma_y^i}{2} - |y|\right), \quad (5)$$

$$\omega_i^{(1y)}(\boldsymbol{r}) = \frac{1}{2}\delta\left(\frac{\sigma_x^i}{2} - |x|\right)\Theta\left(\frac{\sigma_y^i}{2} - |y|\right), \quad (6)$$

$$\omega_i^{(2)}(\boldsymbol{r}) = \Theta\left(\frac{\sigma_x^i}{2} - |x|\right)\Theta\left(\frac{\sigma_y^i}{2} - |y|\right), \quad (7)$$

where δ is the Dirac delta, Θ is the Heaviside step function, and σ_x^i and σ_y^i are the rectangle's length in the x- and y-direction, respectively. These expressions can be combined in a grand canonical free energy equation,

$$\Omega[\rho_i] = F[\rho_i] - \sum_i \int_A dr\rho_i(r)\left[\mu_i - V_{ext}^i(r)\right] \quad (8)$$

which can be minimized using a matrix-free Newton method [78]. The resulting energy minimization will provide two density profiles, $\rho_{\text{horizontal}}$ and ρ_{vertical}, which can subsequently be evaluated for order.

3.3 Results and Discussion

The system we consider models a slowly evaporating suspension of quasi-2D hard rectangular particles (of negligible thickness) on a templated substrate. The suspension is in contact with a flat, 2D surface decorated with chemical or topographical patterns. The barriers impose an energetic penalty to particles that intersect with the centerlines of the template features, which is as step function equal to βV_{ext} if a particle overlaps (where $\beta = 1/k_B T$), and zero otherwise. The particles are free to adsorb and desorb from the substrate in accordance with the chemical potential of the suspension, and so we model the system in the grand canonical ensemble. Furthermore, high chemical potentials require a barrier height sufficiently large to prevent particles from overlapping the template boundary. Thus, all presented simulations set $\beta V_{\text{ext}} = 50$. Similar to the results presented in the previous chapter, we found that this system is not sensitive to small changes in βV_{ext}.

Particles with aspect ratio a = 2.0 were deposited for a template spacing L_x/R = L_y/R = 6.1. As shown in Figure 2(a), these particles are unable to form the desired rectangular array, with the equilibrium structure lacking both translational and orientational order. The snapshot of a typical configuration from a GCMC simulation illustrates tetratic order similar to that of the bulk system in the absence of any template barrier. This occurs due to the rotational symmetry of two-particle clusters. For a = 2.0, two particles can align to form 2Rx2R squares, which can orient either vertically or horizontally without enthalpic penalty or influence from the template. These pairs can manifest in a number of different ways, leading to a far higher probability of finding a tetratic microstate than a horizontally ordered structure. If the horizontal orientation is desired, one must choose the dimensions of the particles and template that penalize states with vertically aligned particles.

This can be accomplished by using fractional particle aspect ratios and adjusting the template spacing in each direction. For example for a = 2.2, particle pairs lose the rotational symmetry found for particles with a = 2.0. Further, the L_y is fixed at 6.1R which is commensurate with horizontal ordering of the particles and penalizes vertically aligned particles. In Figure 3.2(b) we have targeted horizontal particle alignment with L_y = 6.1R, while expanding L_x to 6.9R, which is the proportional increase in particle size in order to accommodate the higher aspect ratio. This adjustment of the particle and template sizes generates the desired translational and orientational order. GCMC results in Figure 3.2(a) and (b) are supplemented by a Fundamental Measure Theory (FMT) model in a DFT prediction of non-overlapping rectangular particles that treats the assembled system as a bidisperse mixture of vertically and horizontally aligned particles. Simulation results suggest that this approximation is valid, as it is rare to find particle orientations deviating from 0º or 90º at high surface coverage. Density profiles of a = 2.0

and a = 2.2 particles are shown in Figure 3.2(c) and (d), respectively. The FMT model predicts a structured 3x6 lattice for a = 2.2 particles in a commensurate template, but no discernable order for a particle aspect ratio of a = 2.0. These results demonstrate excellent agreement between simulation and the FMT model.

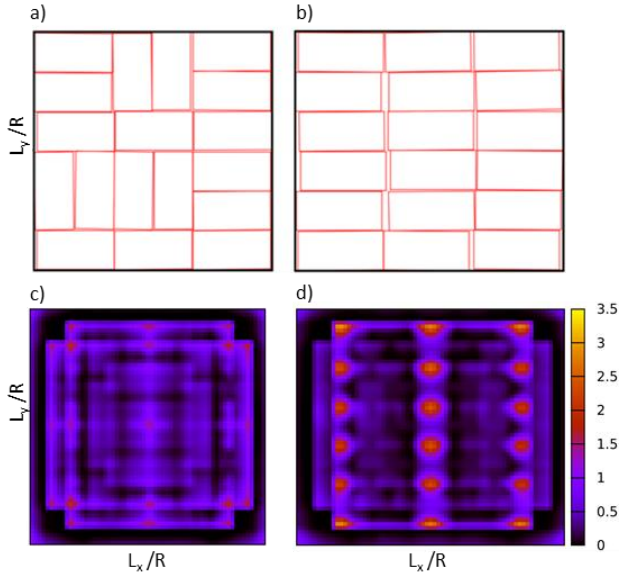

Figure 3.2: GCMC snapshots and FMT density profiles of rectangular particles of (a&c) a = 2.0 and (b&d) a = 2.2 exposed to enthalpic barriers at the edge of each displayed area. For all plots Ly/R = 6.1 while Lx/R is (a&c) 6.1 and (b&d) 6.9. While a = 2.0 particles are free to orient vertically or horizontally without energetic penalty, the rotational asymmetry of a = 2.2 particles can be utilized to generate orientational order. Density profiles are in agreement, showing clearly distinguishable peaks in rectangular lattice coordinates for the a = 2.2 aspect ratio

The separation of the template is next increased for a = 2.2 particles to determine the limits of pattern multiplication on this system. As shown in Figure 3.3, the system exhibits horizontal order for the 4x8 (L_x/R = 9.2, L_y/R = 8.1) and 5x10 (L_x/R = 11.6, L_y/R = 10.1) targeted structures, but reverts to tetratic order for larger wall separation. Note that this maximum wall separation of ~10R is very similar to the limitation on pattern multiplication seen in the hard-sphere system [92]. While this may be indicative of a

physical limitation of graphoepitaxial assembly, it can also be explained from the perspective of packing energies. A line of five vertically aligned a = 2.2 particles requires the same amount of vertical space as 11 horizontally aligned particles. Thus, it becomes impossible to impose a penalty on misaligned particles at larger template spacings, since the particles can arrange themselves in two separate configurations with the same energy.

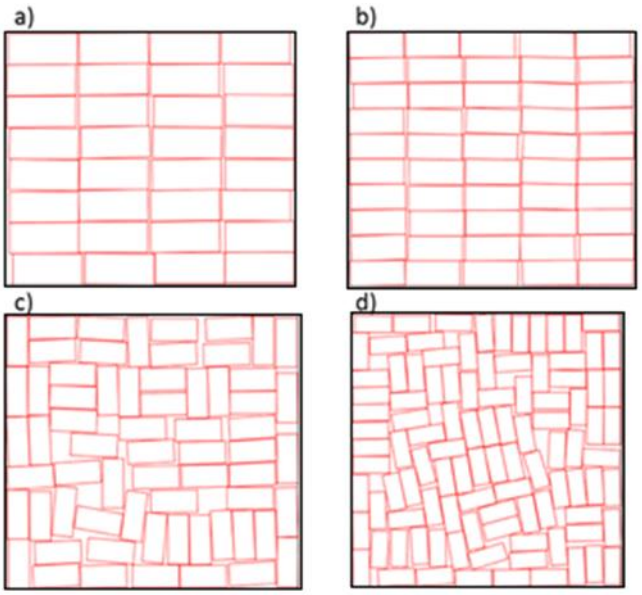

Figure 3.3: GCMC snapshots of a = 2.2 rectangular particles in the presence of walls of increasing separation. Target lattices are (a) 4x8 (b) 5x10 (c) 6x12 (d) 7x14. Template spacings are as follows Lx/R = (a) 9.2, (b) 11.6, (c) 13.9, (d) 16.2 and Ly/R = (a) 8.1, (b) 10.1, (c) 12.1, (d) 14.1. Beyond a wall separation of Ly/R ~10, rectangular order is no longer observed.

A more complete picture of the phase behavior of a = 2.2 and a = 2.7 particles from GCMC simulations and FMT is shown in Figure 3.4. The solid color regions represent the values of L_x/R and L_y/R which yield horizontally ordered structures according to GCMC simulations. Systems are defined to be ordered if the standard deviations in translational position are smaller than 5% of the lattice constant and the standard deviation in the particle orientation is within 5% of desired horizontal

alignment. Furthermore, these boundaries are supplemented by FMT simulations, indicated by green (successfully ordered) and red (unsuccessfully ordered) data points. This approach approximates the rectangular particle system through a bidisperse mixture of vertically and horizontally aligned particles, resulting in two energetically minimized density profiles, $\rho_{\text{horizontal}}$ and ρ_{vertical}. To evaluate order, we utilize an order parameter defined as $Q = \frac{\bar{\rho}_h - \bar{\rho}_v}{\bar{\rho}_h + \bar{\rho}_v}$, where $\bar{\rho}$ represents the density profile integrated over the template area. Positive Q values denote systems predominantly composed of horizontally aligned particles (practically, $Q > 0.5$ represents a strong indication of horizontally ordered structures), while negative values represent vertical alignment. $Q = 0$ is indicative of tetratic order. As shown, the FMT results indicate excellent agreement with Monte Carlo simulations.

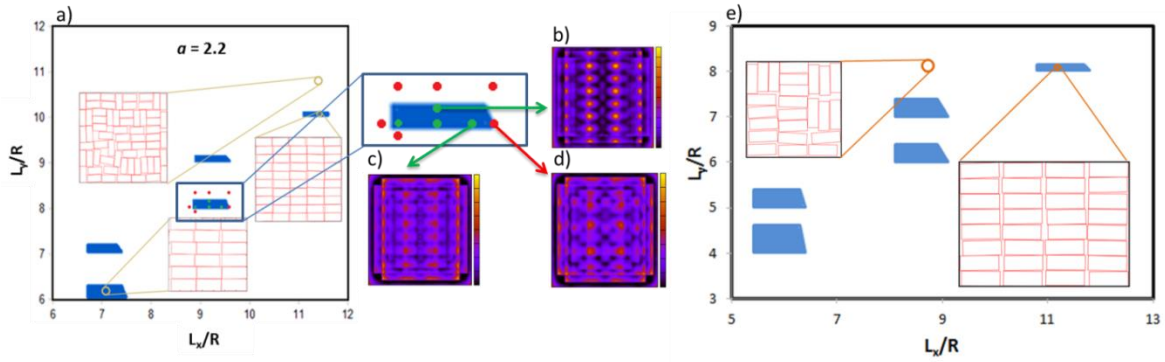

Figure 3.4: A phase diagram of (a) a = 2.2 and (e) a = 2.7 particles as a function of wall separation in the x- and y- directions as computed from GCMC simulations. Shaded areas denote rectangular ordered phases, with representative GCMC snapshots to illustrate achievable lattices. FMT results for the 4x8 lattice are illustrated on (a) as green data points for successful templates and red for unsuccessful templates, showing quantitative agreement with the simulations. Representative density profiles are shown for (a) Lx/R = 9.2, Ly/R = 8.2, resulting Q = 0.62; (b) Lx/R = 9.6, Ly/R = 8.05, resulting Q = 0.53; and (c) Lx/R = 9.7, Ly/R = 9.05, resulting Q = 0.08. All color bars show a density range from 0 to 3.5.

It is important to note that each ordered region in Figure 4 spans a far shorter range of template separations in the *y*-direction than *x*-direction. This suggests that the direction which imposes the penalty on misaligned particles has a tighter restriction on its allowable separation and is the more significant parameter in template design. However, each ordered region for a = 2.7 particles spans a wider range of L_y/R values than we observed for the a = 2.2 particles. This is because the comparatively longer particles require a greater fractional increase in the separation of the template wall in the *y*-direction before a vertically misaligned particle can fit without energetic penalty. It is also important to note that this particular result is only due to our targeting the horizontal alignment. If vertical alignment was desired, the *x*-direction separation would be the limiting factor.

Since the *x*-direction separation exhibits a much wider allowable range, we are able to represent it as a function of *y*-direction separation and particle aspect ratio. Using the formula $L_x = 1.05aN$, where N is the result of rounding $L_y/2$ up to the nearest integer, Figure 5 illustrates which values of L_y and a are able to induce horizontal order. As can be seen, the extent of accessible pattern multiplication varies greatly for different values of a, with a = 2.2 yielding translational and orientational order at a wall separation up to $10R$. Additionally, many of these values differ from the prediction provided from the ideal packing argument. For example, a = 2.4 particles would require five particles in a row to occupy an integer spacing ($12R$), yet these particles do not demonstrate order beyond a wall separation of $5R$. Furthermore, Figure 3.5 illustrates that some aspect ratios are incapable of achieving the desired structure beyond unfavorably short wall separations. An aspect ratio of a = 2.0, for example, would require a wall separation $L_y/R < 2.0$ to generate orientational order, which is a trivial graphoepitaxial template. Figures 3.4 and 3.5 show that there are limited islands in the parameter space where orientational

and translational order are achievable. Despite utilization of commensurate template geometries that mimic the rotational asymmetry of these particles, degenerative orientational states limit the extent of pattern replication attainable in the hard rectangle system.

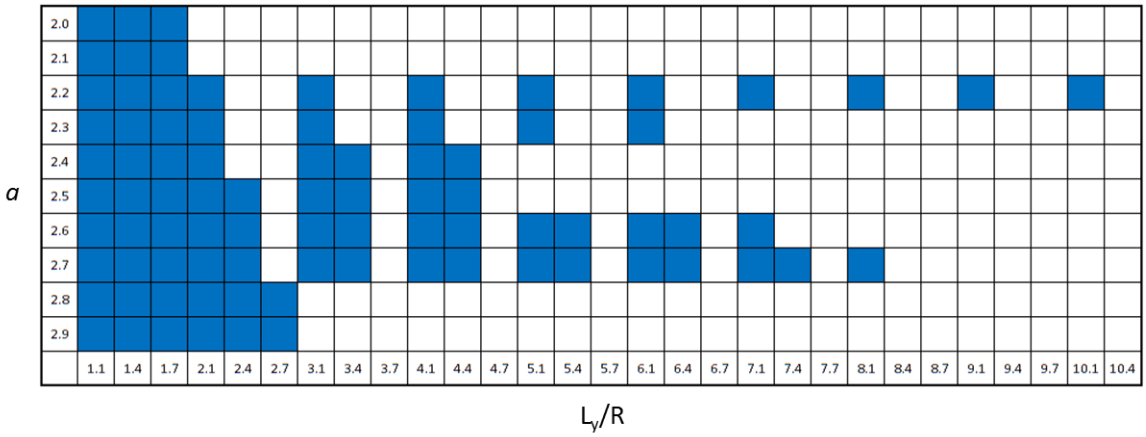

Figure 3.5: Phase behavior of rectangular particles as a function of a and Ly/R. Blue regions are ordered phases, while white represent disordered structures. For each simulation, Lx = 1.05aN, where N is the result of rounding Ly/2 up to the nearest integer. The most promising results appear for a = 2.2 particles, which forms a rectangular lattice for a maximum wall separation of Ly = 10.1R.

3.4 CONCLUSIONS

It has been predicted through GCMC simulations and FMT calculations that rectangular particles can be ordered using graphoepitaxy provided the right combinations of the size ratio of the particle and the size of the template are chosen. The range of these combinations that lead to translational and orientational order have been mapped and shown to be islands determined to penalize alignment in one direction relative to the other. These islands are large enough that the graphoepitaxial process is robust to

practical variations that may occur in particle size distribution and template spacing. Considering only particle shape and template spacing, a maximum pattern multiplication of about 10 times the smaller dimension of the rectangular particle is achievable. The inclusion of soft-repulsions to the interparticle interactions and non-rectangular patterns for the template could increase the maximum allowable wall separation and resulting pattern multiplication.

Chapter 4: Graphoepitaxy Using Open Template Geometries

4.1 Introduction

To this point the focus has been on closed template geometries which completely confine nanoparticulate systems. There remains an open question regarding the necessity of continuous wall templates and whether alternate geometries can have the same effect. The interest in this problem is two-fold. Open template structures can provide insight to the true limits of pattern multiplication that can be achieved in hard particle systems. With sparser open features the impact of the external field decreases and interparticle interactions assume a larger role in propagating long-range order throughout the system. Furthermore, the primary motivation of this project is to limit the magnitude of top-down nanopatterning in nanofabrication processes. Such templates have been demonstrated to have varied levels of success for block copolymer systems [93-96] and particulate systems [97-99]. We aim to investigate the feasibility of reducing the prepatterning and thus decreasing the cost of the fabrication. Here we study a variety of templates, comprised of truncated walls and fixed particle posts and evaluate their ability to generate square order.

4.2 Simulation Methods

Simulations in this chapter explore systems of hard spheres and hard rectangles, identical to the particles studied in Chapters 2 and 3. Thus, work here employs similar GCMC and FMT techniques detailed in previous chapters. For hard sphere particles, we utilize a simulated tempering algorithm [100] which is beneficial for high density

systems, as it allows for limited particle overlap early in the simulation, and reaches a true hard sphere model after a prescribed number of Monte Carlo steps. Rectangular particle results in this chapter utilize both the FMT and growth-expanded GCMC techniques detailed in Section 3.2. As in previous chapters, length scales here will be represented in terms of a variable R, which denotes the radius of a spherical particle or the short side of a rectangular particle.

Template-particle interactions are represented by mathematical step functions, with an enthalpic pentalty of βV_{ext}, set to 10 for hard spheres and 100 for hard rectangles. Difference in magnitude of βV_{ext} for these systems is due to the high chemical potential required for close-packing of hard rectangles. With higher chemical potential, barrier height must be increased to prevent inserted particles from overlapping the enthalpic barriers. These field interactions act on particle centers, meaning that an infinitely thin physical barrier would be represented by a step function of width $2R$, in the case of hard spheres.

4.3 Results and Discussion

4.3.1 Truncated wall templates for spherical particle monolayers

The results discussed in Chapter 2 show that a template comprised of perpendicular walls separated by a distance commensurate to an integer multiple of particle diameter was sufficient to assemble spherical particles in a square lattice. Our investigation into open templates begins with a truncation of these template walls by removing segments in the middle of each feature. These truncations are then expanded by integer multiples of the particle diameter. Gaps increase in size until the square symmetry is no longer observable.

Templates are studied through grand canonical Monte Carlo simulations, where chemical potential is a determinate parameter for particle density in the system. This value, denoted $\beta\mu$, is set to $\beta(\mu-\mu_{hcp}) = 5.87$, which was observed to be sufficient to yield defect free square structures with the closed template geometry as illustrated in Figure 2.4. Figure 4.1 illustrates the truncated templates for 10x10 target structures, with gaps of $2R$, $4R$, and $6R$ in length. As the openings increase beyond $2R$, lattice fidelity clearly begins to deteriorate from the desired square pattern. For $4R$ and $6R$ gaps, rows and columns of the square lattice are able to freely translate, leaving structures with square symmetry in the corners near the template features, and quasi-hexagonal order far from the enthalpic barriers.

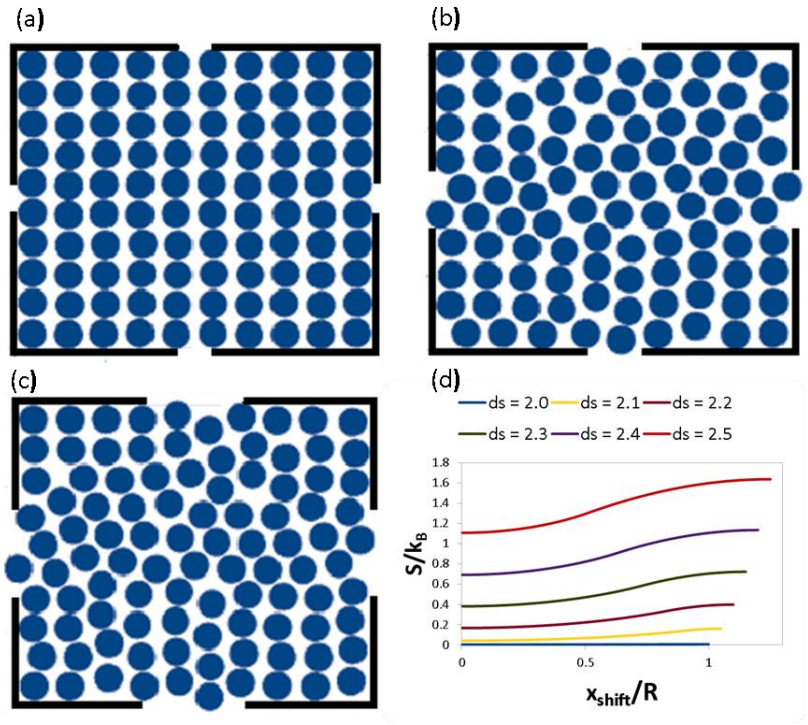

Figure 4.1: GCMC snapshots of hard spheres exposed to a 2D square template, with gaps of (a) 2*R*, (b) 4*R*, and (c) 6*R* in each wall. The black boundary represents an external field of $10k_BT$ and periodic boundary conditions are applied. As the gaps in the walls widen, rows and columns are free to translate away from the square lattice, leaving a disordered structure. The per particle entropy increase of this row/column translation is illustrated in (d), where the free volume of a single reference particle is used to calculate S/k_B as a single row containing the test particle is moved a distance x_{shift}. Various curves represent increases in the lattice constant, d_s, of the initial square lattice structure. Unsurprisingly, entropy is highest for a row that shifts 1*R* away from the ideal square coordinates.

This phenomenon can be explained through a simple entropic argument. For systems of hard particles, assembled structures form by maximizing free volume per particle, which in turn increases available microstates. Figure 4.1(d) demonstrates this through a cell theory approximation of entropy per particle [101]. This simplified

calculation determines entropy through a free volume calculation for a reference particle with fixed nearest neighbors. Further detail for this method is outlined in Section 5.2. For the results in Figure 4.1(d), a square structure with a lattice constant d_s is fixed surrounding a reference particle in a freely translating row. Free volume for this particle is calculated as its row translates out of phase with the target square lattice. This is performed for structures with lattice constants of $d_s = 2.0R$ through $d_s = 2.5R$. As shown, the entropy is at a minimum when the row is perfectly aligned and at a maximum when it lies between square lattice coordinates. This entropic favorability explains why we see free translation of rows and columns without sufficient confinement.

Results in Figure 4.1 highlight the necessity to confine each row and column of the square lattice for energetically favorable assembly. It is possible to accomplish this with open templates by constructing a pattern of staggered "+"-shaped features, as illustrated in Figure 4.2. Each feature is composed of four wall segments, each an integer multiple of the particle diameter. Barriers are offset such that the edge of one wall segment occupies the same x- or y-coordinate as a neighboring feature. As shown in Figure 4.2, wall segments of $4R$ are able to direct assembly into square structures, while segments $6R$ in size exhibit disordered structures. This order-disorder transition is noteworthy due to the maximum separation between features for the $4R$ and $6R$ segments. For the former, the maximum distance between walls along any row or column is $16R$, while the analogous distance for the latter is $24R$. This pattern multiplication limit is in agreement with previous work, showing that hard sphere assembly cannot be directed by template features separated by more than $20R$, or ten times the particle diameter.

It is worth noting that increasing chemical potential for the system in Figure 4.2(b) will not result in an ordered system as it did in Figure 2.5. It is evident that particles in this truncated wall template begin to overlap the barriers for sufficiently large

wall separation. This effect is further explained in the following chapter, but can be concisely explained through a trade-off of an increase in entropy for local hcp order versus an enthalpic penalty for a few particles overlapping a template feature. For large wall feature separation, a single particle overlapping a barrier can make room for many more particles to take advantage of the energetically favorable hcp structure. Thus, increasing chemical potential would increase the number of particles which overlap template barriers since the relative enthalpic penalty is much lower than the chemical potential benefit of inserting a particle. Simulations yielded no combinations of chemical potential and barrier height (βV_{ext}) resulting in ordered systems for the template illustrated in Figure 4.2(b).

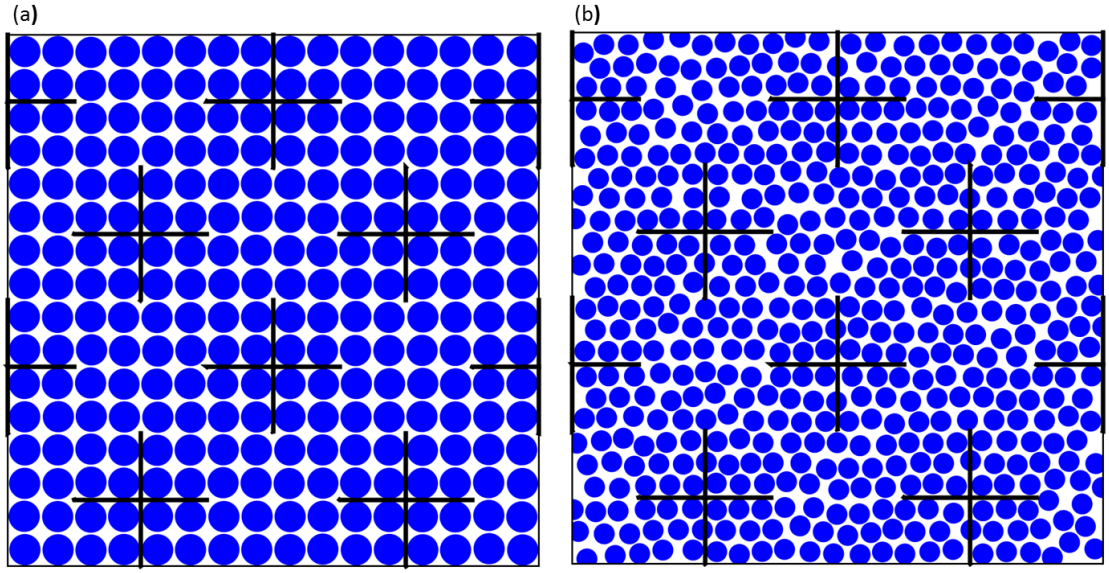

Figure 4.2: Achieving the square lattice requires that the template confine each row and column to prevent translation. The above geometry (shown in black) presents a means of utilizing discontinuous features while preserving square order. The truncated walls represent a length of (a) 2D and (b) 3D. It is important to note that the order-disorder transition from (a) to (b) occurs between a maximum template feature separation of 8D and 12D, which agrees with previous results showing a limit of 10 times the particle dimension for graphoepitaxial assembly.

4.3.2 Truncated wall templates for rectangular particle monolayers

Results presented in Chapter 3 demonstrated that successful graphoepitaxial assembly is also achievable for hard rectangular particles [102], which may be used as templates or directly for bit-patterned magnetic media. To study the effects of open template geometries on these anisotropic particles, we use templates analogous to those used in Figure 4.2, adjusted for commensurate length scales of aspect ratio a = 2.2 rectangular particles. The FMT model outlined in Section 3.2 is used to explore this directed self-assembly due to computational efficiency of the technique.

FMT results shown in Figure 3 demonstrate that wall segments of $2R$ in the y-direction generate sufficient order, while segments of size $3R$ do not. Similar to the hard sphere results, this corresponds to a maximum feature separation of $8R$ for a successful template and $12R$ for an unsuccessful one. Once again, this agrees with previous work which found a limiting pattern multiplication factor of $10R$ for rectangular assembly. It is apparent that entropic assembly of square or rectangular lattice is possible regardless of template geometry, provided that each row and column is exposed to confinement within ten times the particle size.

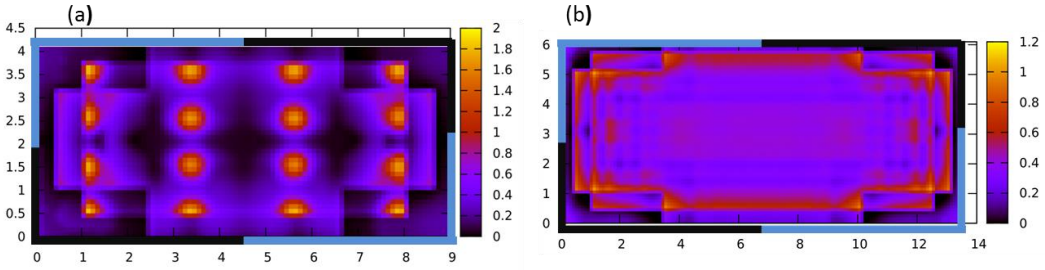

Figure 4.3: FMT profiles of rectangular particles of aspect ratio a = 2.2 exposed to the same "+"-shaped templates illustrated in Figure 2. Barriers are place in the lower left and upper right corners (indicated by black edges), with symmetric boundary conditions applied (indicated by blue edges). Wall segments are $2R$ (a) and $3R$ (b) in the y-direction and $2aR$ (a) and $3aR$ (b) in the x-direction. Template features separated by a maximum of $8R$ (a) are able to generate rectangular order, while features separated by $12R$ (b) exhibit a more uniform density profile, indicating tetratic order.

4.3.3 Fixed particle post templates

Truncation of wall features is ultimately investigating the ability of particles to impart long range wall effects through local packing. Each template feature is influencing particles to align along the wall, with further order arising from subsequent layering around particles in contact with the barrier. Thus, a natural question arises whether stationary particles fixed at target lattice coordinates can generate the same pattern multiplication as continuous or truncated walls. We thereby construct templates consisting of particles fixed at locations commensurate to the target square (or rectangular) structure, with the aim of serving as seeds for the assembly of the desired lattice.

Figure 4.4 illustrates the effect fixed spherical particles arranged in a sparse square symmetry, with both aligned and staggered geometries. In each case, templates are unable to induce square lattice formation, resulting in disordered structures. Template features were additionally altered to be squares of side $2R$ in an attempt to direct local

packing into a four-fold symmetry, but ultimately these geometries were unsuccessful as well. It is important to note that these templates reach a lower areal fraction than previously studied systems at the same chemical potential. This is due to a loss in entropy incurred by restricting the vibrational entropy of the fixed template particles. Simulations shown were conducted at a chemical potential 50% higher than those in Figures 2.5(c), 4.1 and 4.2, but still result in a lower system density. Melting simulations were also conducted, with initial configurations matching the target lattices, and each case produced equilibrium structures similar to those shown in Figure 4.4.

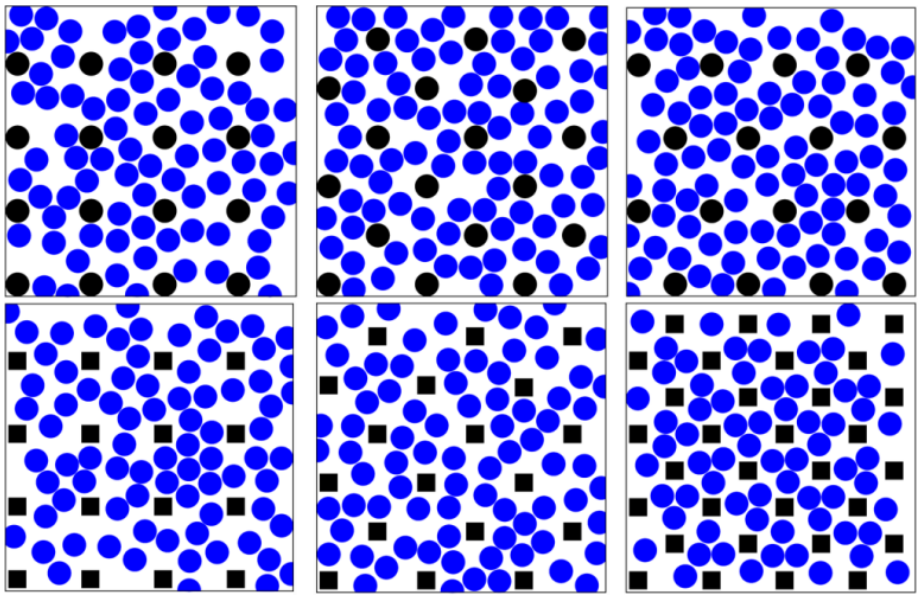

Figure 4.4: GCMC snapshots of hard spheres exposed to fixed posts of different geometries. A number of different post configurations were tested, with no observed square lattice formation. Square posts showed no improvement over circular posts in their ability to generate square order. Additionally, the immobile posts had a large effect on the observed density of the system, resulting in packing fractions far below those of hcp lattices at equivalent chemical potential.

Templates of fixed rectangular particles demonstrate more successful alignment than spherical monolayers, as shown in Figure 4.5. Efficient particle packing allows

template effects to more easily propagate through the system. Rectangular arrays of fixed particles are observed to generate columnar order for sufficiently close posts, with tetratic order prevalent in between. However, patterns of diagonally fixed rectangular particles are able to generate full rectangular lattices between template features. This order is observed for templates which fix every fifth particle in the target lattice, and transitions to disorder when every sixth particle is confined. Note that this periodicity leads to a feature separation of ~10R for a = 2.2 rectangular particles, once again illustrating a pattern multiplication limit up to ten times the size of the particle.

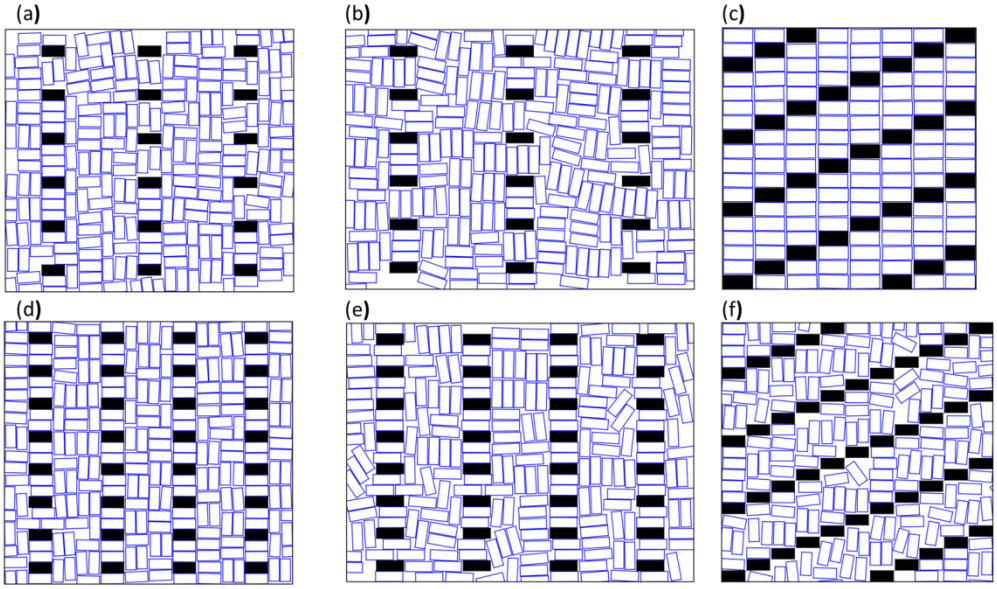

Figure 4.5: Snapshots of freely rotating and translating hard rectangular particles (blue) exposed to templates of fixed posts (black). Aspect ratios are a = 2.2 for (a), (c), (d), & (f) and a = 2.7 for (b) & (e). The anisotropy of the rectangular geometry allows these templates to generate more order than the spherical posts. This is most prevalent in the columnar order in (d), where particles align along the columns of the template forming tetratic order in between, and in the rectangular lattice in (c), where the confinement of each row and column is sufficient to generate the desired order. Note that this template effectively fixed every fifth particle horizontally, which amounts to a 10R feature separation for a~2 particles. This once again agrees with previous work on the limits of pattern multiplication in particle assembly.

4.4 Conclusions

Open template geometries have demonstrated ability to direct assembly of spherical and rectangular particles into square and rectangular lattices, respectively. GCMC and FMT simulations showed that confinement of every row and column of the target lattice is necessary for truncated wall templates and fixed rectangular particle templates. Entropic effects reduce lattice fidelity through free translation of locally unconfined particles. However, with proper confinement, template features can consistently be separated by distances ten times greater than particle size, which is consistent with observed pattern multiplication limits of closed template geometries.

Chapter 5: Cell Theory Insights into Pattern Multiplication Limits

5.1 Cell Theory Approximation

Chapters 2 through 4 demonstrated that hard particles could be caused to assemble into square/rectangular structures at high areal fractions in the presence of prepatterned templates which favored these particle arrangements. In each case, however, there was a template length scale above which defect-free pattern multiplication could no longer be induced by template features (i.e., graphoepitaxy fails for sufficiently sparse template features). Surprisingly, this limiting value was consistently shown to be approximately ten times the particle size, irrespective of the specific template or particle geometry. Density multiplication limits of similar magnitude have additionally been observed in block copolymer systems [103,104]. The ubiquity of this value across different systems leads to an obvious question. Why does such a limit to pattern multiplication exist?

To get physical insight into this ubiquitous length, we turn to a simple cell theory approximation of entropy. This formalism, originally introduced by Lennard-Jones and Devonshire [105] and further developed by Hoover et al. [106,107], calculates entropy of dense phases by considering a multiplicative partition function of single particles in "cells" with boundaries defined by the presence of their neighboring particles. Cell theory has been able to generate hard particle equations of state [108-110] and predict phase behavior [111,112]. Here, we utilize this approximation through a configurational contribution to entropy through the integrals

$$Q_N = \frac{1}{\lambda^N N!} \int \exp\left(\frac{\Phi}{k_B T}\right) dr^N. \qquad (1)$$

For hard particles, $\exp\left(\frac{\Phi}{k_B T}\right)$ will be either 0 or 1, resulting in $Q_N = \frac{1}{N!}\left(\frac{v}{\lambda^N}\right)^N$ assuming N independent cells of volume v. This cell volume is defined by the available space for a reference particle confined by fixed neighbors in specific lattice coordinates. Exact cell volumes have been determined for a variety of structures in 2D [113] and 3D [114]. For the 2D structures in this work, we focus on cell volumes confined within hexagonal and square lattices. These volumes, diagrammed in Figure 5.1 below, are calculated using $2R$ exclusion areas surround each neighbor particle. Cell volume is dependent on the lattice constant of the neighbor particles, which is defined as the variable d. These constructions then allow us to compare the Helmholtz free energy difference of the hexagonal and square lattice through:

$$\Delta F = \Delta U - T\,\Delta S \qquad (2)$$

where, $$\Delta S = k_B \ln\left(Q_N^{hcp}/Q_N^{sq}\right) = N k_B \ln(v_{hcp}/v_{sq}). \qquad (3)$$

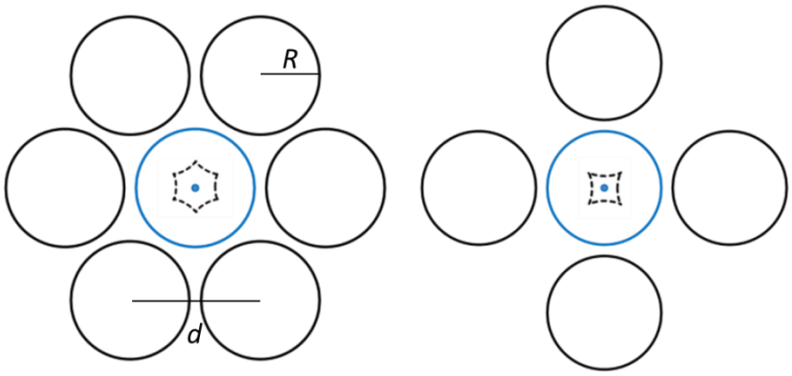

Figure 5.1: Illustration of the cell volume for single reference particles in a (a) hexagonal lattice (left) and a square lattice (right). The cell volume, v, is determined by constructing an exclusion area of $2R$ around each neighbor particle. The boundary traced by the dashed line represents the free volume a reference particle has without overlapping with any of its neighbors.

5.2 Enthalpic Penalty of Overlapping Particles

We first compare the Helmholtz free energy of defect-free hexagonal and square lattices at the same areal fraction in the presence of the template. A perfect hexagonal lattice has an areal packing fraction (η) dependent on lattice constant, d_{hcp}, which is represented by:

$$\eta_{hcp}(d_{hcp}) = \frac{2\pi R^2}{d_{hcp}^2\sqrt{3}} \qquad (4)$$

Similarly, the square lattice packing fraction as a function of lattice constant d_{sq} is:

$$\eta_{sq}(d_{sq}) = \frac{\pi R^2}{d_{sq}^2} \qquad (5)$$

Thus the lattice constant for hexagonal packing at the same areal fraction as a corresponding square lattice is:

$$d_{hcp}^2 = \frac{2d_{sq}^2}{\sqrt{3}} \qquad (6)$$

The former is larger than the latter to its more efficient packing arrangement and hence its larger free volume. Space between template features is thus defined as L, which is an integer multiple of dsq. For consistency with previous simulation results, we choose dsq = 2.1, which is the same value found to induce square order in Figures 2.5 and 2.6. The corresponding hexagonal lattice, which will have a lattice constant of d_{hcp} = 2.26, is then overlaid on a periodic template of enthalpic barriers of height βV and distance L. An example packing is illustrated in Figure 5.2. Due to variability in the number of overlapping hcp particles in a single periodic cell as a function of lattice placement, we construct a long-range system composed of 100x100 confined areas, and take an average number of overlapping and non-overlapping particles per well. This proportion of

perimeter particles (N_p) to total particles (N) is shown in Figure 5.3. Particles overlapping the template features incurred a dimensionless energetic penalty $N_p\beta V$, which is captured in the system's internal energy, U. Figure 5.4 below shows the difference in Helmholtz free energy between hcp structures with boundary overlap and square structures with no template overlap. For close walls (small L), the hcp lattice exhibits higher free energy as compared to the square lattice, but there is decline and crossover as the template features become sparser. This trend is due to the linear increase in perimeter particles with L, but the quadratic increase of total particles in the system. As the template features expand, a smaller proportion of particles incur a penalty by overlapping the boundary, thus allowing the favorable entropic contribution of the interior hcp particles to surpass the enthalpic contribution of the perimeter particles. Figure 5.4 also demonstrates that pattern multiplication effects are dependent on the barrier height in this model. It is interesting to note that the transitional value for 10x pattern multiplication occurs for $\beta V = 15$, which is similar in magnitude to the requisite $\beta V = 10$ barriers utilized in Chapter 2.

However, we previously found that increasing $\beta V_{ext} > 10$ did not improve square lattice fidelity. In fact, due to the construction of these overlapping hcp lattices in our model structures, one can envision a limit as $\beta V_{ext} \rightarrow \infty$ where even a single overlap would make the square lattice energetically favorable compare to the hcp structure at any wall separation. This limitation on the cell theory model forces us to introduce an ability for particles to rearrange themselves near the barrier to avoid dependence on the βV parameter. This will be detailed in the following section.

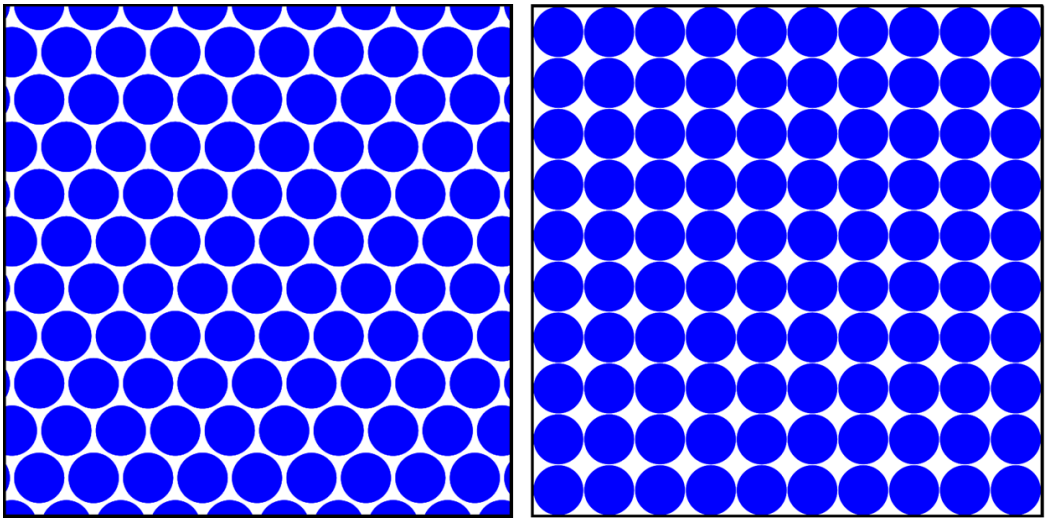

Figure 5.2: Example hcp (left) and square (right) lattices in the presence of a square wall template. Wall features are separated by a distance of 21R, commensurate to a 10x10 square lattice with lattice constant ds = 2.1. The hcp structure at the equivalent areal fraction has a lattice constant dhcp = 2.26 and demonstrates a significant number of particles overlapping the template features, thus incurring an enthalpic penalty of $N_p \beta V$. Due to the commensurate template geometry, the square lattice incurs no such penalty.

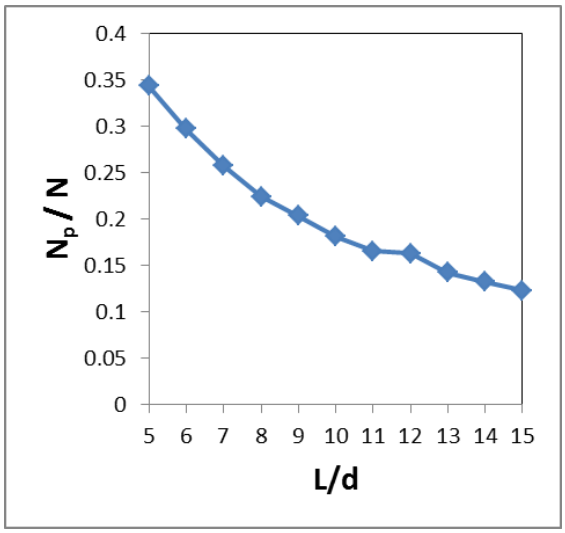

Figure 5.3: Ratio of particles in the hcp structure overlapping the square boundary (N_p) to the total number of particles per confined well (N). As the wall separation L/d increases, the proportional number of particles overlapping the template feature decreases, allowing the entropic benefit of interior particles to surpass the enthalpic penalty of perimeter particles.

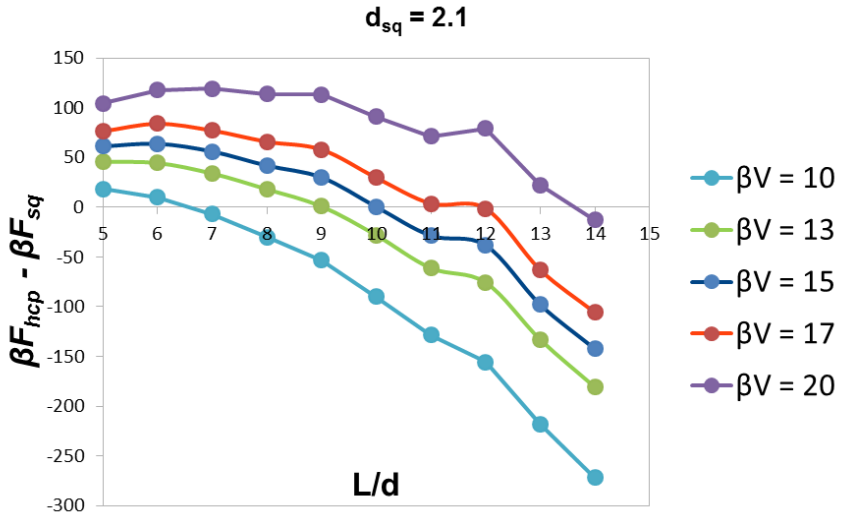

Figure 5.4: Difference between Helmholtz free energy (βF) of the hcp and square lattices for square templates commensurate to a lattice constant d_{sq} = 2.1. Hexagonal particles overlapping with the template incur an energetic penalty of βV, thus increase the free energy of that structure. As the template features are further separated, the proportional number of particles affected by the boundary decreases and the entropic benefit of hexagonal packing prevails. The exact location of this transition is dependent on the barrier height, but is consistently near the 10d value predicted for previously discussed systems.

5.3 Confined Boundary Particles

While the boundary overlap model suggests order of magnitude agreement with previous results, it is not necessarily indicative of the true packing. It would be possible for particles to assemble into a quasi-hexagonal structure without any enthalpic penalty. For this case, the free energetic cost would be an entropic penalty due to confinement of particles due a disturbance in the otherwise favorable hcp packing geometry near the boundary, an effect which counterbalances the more efficient packing of the hcp lattice in the interior. To model this, we divided the hexagonal unit cell in half, in order to capture the confinement of particles near the wall. This unit cell is illustrated in Figure 5.5 and

will result in a free volume v_c. We also estimate that these particles would be significantly more confined, and attribute a new interparticle distance d_c to sufficiently restrict the movement of boundary reference particles. Considering cell volume to be a function of the lattice constant, $v(d)$, we can rearrange the entropy expression in equation (3) to be:

$$\Delta S = k_B \ln \left[\frac{v_c (d_c)^{N_p} \, v_{hcp} \left(d_{hcp}\right)^{N-N_p}}{v_{sq} \left(d_{sq}\right)^{N}} \right] \quad (7)$$

For each value of feature separation, $L = nd$, we designate a set number of particles as confined perimeter particles. Assuming these boundary particles form a single layer against each wall, this will result in $N_p = 4n\text{-}4$ particles under the confined conditions, with the remainder receiving the benefit of full hexagonal cells. Figure 5.6 illustrates how the extent of pattern multiplication is affected by chosen value of d_c. Once again, with tight confinement of boundary particles, we see that the maximum template feature separation is approximately $10d$.

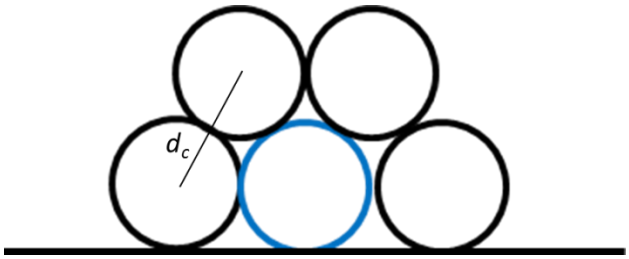

Figure 5.5: A unit cell of a boundary particle in a system with inefficient packing. Interparticle distance is set to be some value $d_c < d_{hcp}$ to represent tighter confinement near the walls.

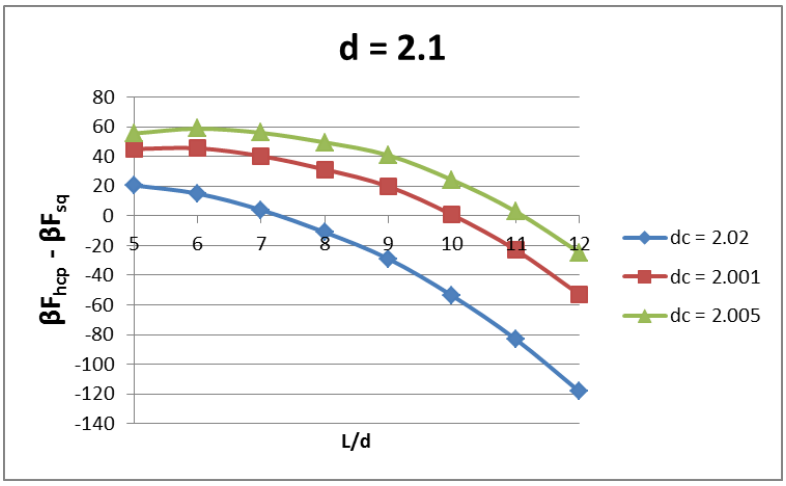

Figure 5.6: Helmholtz free energy difference between hcp and square packing in the presence of a hard wall template where walls are separated by an integer multiple of d_{sq} = 2.1. Boundary particles are confined to a cell surrounded by particles separated by an average distance of d_c. The exact value where hcp becomes the entropically favored structure varies with d_c, but is once again seen to be around $10d_{sq}$.

It is interesting to note that it is possible that rearrangement of the boundary particles could result in a reduced free volume per particle than the hexagonal packing studied here. If we consider disordered systems in the presence of a walled template (see Figures 2.8(b) and 4.2(b)) to exhibit random close packing (rcp) as opposed to hcp plus a confined boundary layer, cell confinement effects could be further exaggerated. This rcp structure is known to occur at lower packing fractions than hcp [115], meaning that individual particles in these systems have a lower free volume than their hcp counterparts at the same density. In this section, we choose to consider hexagonal packing as it is the most efficient packing and thus the wisest choice when evaluating a competing structure. However, if rcp prevails, it would suggest that d_c for this system is smaller than the values studied in the hcp boundary layers. Furthermore, random close packing through the system would mean that these confinement cells are not solely limited to the periphery, exacerbating the free energy penalty demonstrated above.

5.4 CONCLUSIONS

Using a cell theory approximation of the Helmholtz free energy, we are able to discern an estimate for the maximum template wall separation for which square structures are thermodynamically favorable. Utilizing two models of imposing energetic or entropic penalties on hcp structures due to the boundaries, we find that the transition to hcp favorability occurs around $L = 10d$. This is largely due to the proportion of perimeter particles which are exposed to an energetic or entropic free volume penalty decreasing with template spacing. As template features become sparser (L increases), boundary particles increase linearly, while the total number of particles increase quadratically. For widely spaced walls, interior particles contribute an increase in entropy sufficient to offset energetic or entropic restrictions placed on the packing by boundaries, which limits the scale of template induced pattern multiplication.

Chapter 6: Conclusions and Future Work

6.1 Summary

This dissertation explores a number of ways to use templates to induce specific types of order into self-assembled particle monolayers. Hard spherical particles were shown to assemble into a square lattice, which is not normally entropically favorable, when a commensurate template was applied to the system. This template was able to generate 10x pattern multiplication simply through the propagation of wall effects. A similar method was applied to force hard rectangles to assemble into a target structure of translationally and orientationally aligned particles. Through control of particle aspect ratio and template commensurability, we were able to once again achieve 10x pattern multiplication. This technique was carried over to open template geometries (i.e., "posts"), where truncated wall templates were shown to generate similar pattern multiplication effects, provided they confined translation of each row and column of the square lattice. Additionally, a cell theory approximation provided insights into the competition between entropic benefits of local hexagonal order and energetic/entropic penalties form template features.

6.2 Conclusions

The primary contribution of this work was the demonstration of templated self-assembly for particles lacking any enthalpic interparticle interactions. Through geometric influence of particle packing, we were able to achieve structures that would not otherwise be favorable. Furthermore, we found a consistent limit of pattern multiplication as ten times the particle size for assembly in these systems. This can have

a significant impact on the design of new nanomanufacturing processes, as it will be possible to pattern on a coarse length scale and achieve order ten times finer than the initial template. This combination of top-down and bottom-up nanomanufacturing could lead to more cost efficient processes, while also providing a method of directly fabricating functional nanomaterials. Additionally, inclusion of these periodic, prepatterned substrates could prove to be a key tool in the fabrication of long-range, defect-free nanopatterns necessary for a variety of applications.

6.3 Future Directions

6.3.1 Experimental Validation

Work presented to this point has been exclusively computational, and makes a number of simplifying assumptions in order to investigate the basic physics of templated assembly processes. Ultimately, the goal of this project is to provide instructions for template construction for new nanomanufacturing techniques. Future implementation requires an even greater understanding of these systems from both practical and theoretical perspectives. Experiments to validate the predictions of simulations are needed. Initial investigations should be focused on the systems of spherical particle monolayers as presented in Chapter 2. The basic experimental procedure is outlined in the schematic shown in Figure 6.1.

These experiments will provide a number of vital insights that were unable to be studied through the previous simulation. Firstly, the hard sphere particles studied are an approximation that would be difficult to perfectly replicate in the lab. Prevalence of van der Waals forces at short length scales introduces an enthalpic component increasing in importance for particles as small as 10nm. Furthermore, colloidal particles often have

stabilizing ligands and small surface charges which cause them to deviate from the hard sphere interaction model. The proposed experiments will elucidate whether these short range additions to the pair-wise interaction have a significant impact on equilibrium structures.

Further challenges in monolayer deposition lie with the dynamic components of the assembly process. As previous work has focused on energy minimizing structures, it is unknown whether such particle confinement will lead to dynamic arrest hindering the assembly of the target structure. Furthermore, there are a number of challenges in assembling a single, uniform monolayer which allows particles to freely move toward the energetic minima [116]. Future experimental procedures will need to address this and suggest a deposition technique which can predictably generate long-range, defect free assembled structures.

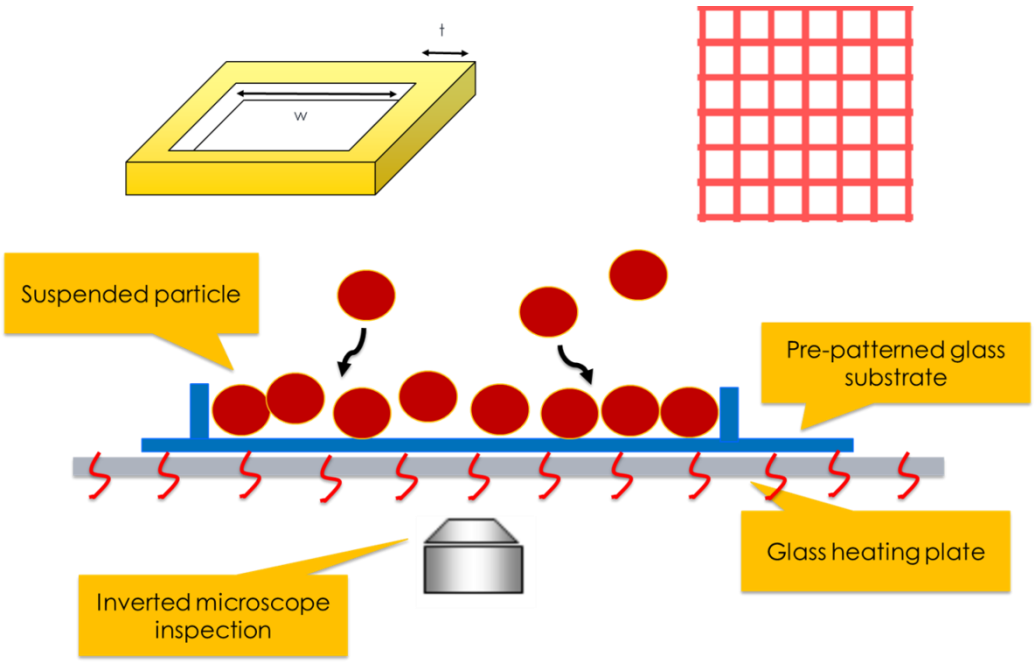

Figure 6.1: Schematic of the experimental apparatus used to study the assembly of spherical particle monolayers. Template features are constructed by etching a glass substrate into various wells of width w, where w will span distances $4D$ to $20D$ in length. Wells will be arranged into a continuous grid as shown above in red. Each adjacent well will be separated by a topographical barrier or a thickness $t = 1\mu m$, which will provide the necessary confinement for assembly. Particles 1 μm in diameter will be exposed to the substrate via an evaporating suspension. Speed of evaporation will be controlled through a heating plate. This solvent evaporation will serve to increase chemical potential in the suspension as particles become more concentrated, thus driving more particles to the substrate. Each well will then be evaluated by its ability to direct assembly into a square monolayer. Figure courtesy of X. Zhu.

6.3.2 Enthalpic Interparticle Interactions

Self-assembly of particulate systems is not limited to entropic forces alone. While entropy will always influence assembly, either toward or away from some target structure, there are a plethora of ways to design interactions which utilize enthalpic energy minimization for the formation of equilibrium lattices. As mentioned in Chapter 1, these interactions can take any number of forms, from amphiiphilic Janus particles, to

DNA linking ligands. It is even possible to further simplify these interparticle interactions through optimized polymer ligand coatings over hard sphere cores.

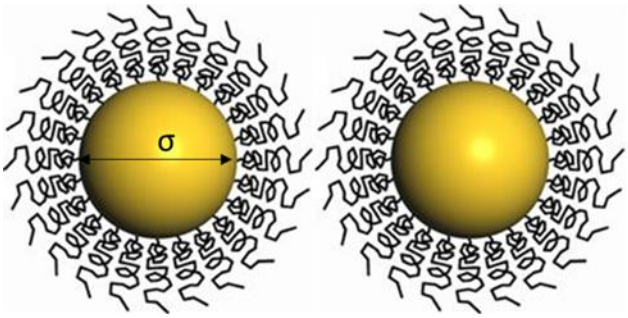

Figure 6.2: Illustration of ligand-coated nanoparticles. Interactions are defined by contributions to steric, osmotic, and Van der Waals forces, and can be controlled by tuning parameters including grafting density, ligand molecular weight and Hamaker constant. This figure is reproduced from R. Tiruvalem et al., J. Phys: Conference Series 371, 012028 (2012) [117].

Previous work by Avni Jain and coworkers demonstrated that optimized pair potentials can allow particles to assemble a wide variety of lattice structures [118,119]. Using a parameterized model for polymer ligand interactions, it was possible to decrease the free energy difference between hexagonal and square structures. While these optimizations did not appear to generate stuctures with square order, they were able to provide a sufficient favorability for an enthalpic template to overcome the energy difference. Figure 6.3 below illustrates Monte Carlo snapshots of these optimized particles in the presence of the same square template investigated in Chapter 1. However, due to the inclusion of optimized enthalpic interactions, the allowable wall spacing was able to be doubled while still preserving square order. This promising result suggests that soft interactions may increase template pattern multiplication effects, and should be investigated for various types of interactions (ligand coatings, charged particles, etc.). The primary challenge of templated assembly of soft particle systems appears to be the

ambiguity of a commensurate length scale for a target lattice structure. For hard particles, template design is straightforward with barriers separated by an integer multiple of particle size. Inclusion of soft interactions, however, means that there can be greater variability in lattice periodicity, thus requiring more computationally intensive investigations to adequately survey the parameter space of template geometry.

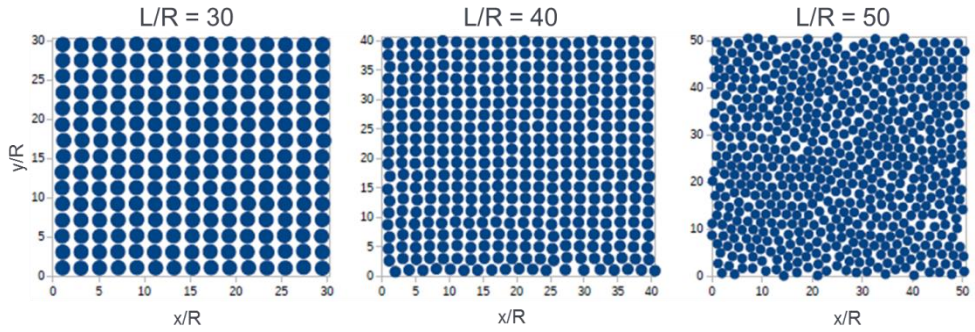

Figure 6.3: Monte Carlo snapshots of optimized soft-particle interactions in the presence of enthalpic barriers. In each plot, barriers are placed at the edge of the displayed simulation area, with periodic boundary conditions applied. Square symmetry is evident for wall separation of L/R = 40, or twenty times larger than the particle diameter. This shows that enthalpic interactions are able to increase the maximum pattern multiplication by a factor of two over the hard sphere systems. However, systematic construction of directing templates has proven difficult for soft particles due to challenges in predicting equilibrium lattice commensurability. Further work is needed before one can formulate design strategies for templated assembly of soft nanoparticles.

6.3.3 Inverse Optimization of Template Features

Figure 6.4: Self-assembly can be approached in two separate ways. First is the more traditional forward approach, where one knows the interactions between particles and field, and uses that information to determine what equilibrium structures are able to form. The second technique, which has gained recent interest, is the inverse approach, where the desired configuration is known, and one must determine the necessary interparticle/field interactions that would lead to formation of the target lattice.

Similar to the inverse optimization resulting in the pair potentials explored in the above section, it is possible to use an inverse approach to self-assembly to design external fields required to assemble target structures. This differs from the forward approach to self-assembly in that the desired equilibrium structure is already known, and the necessary interparticle interactions or external fields are left open. One of the main appeals of using density functional theory to study the assembly process is its potential to incorporate this inverse approach. This technique has already been used for calculating energy minimizing pair potentials [120], but this technique is still unexplored for optimized template design. To accomplish this, one may turn to equation (11) in Section 2.2. This expression of free energy is a function of the density profile, which is a known for some target structure, and a spacially dependent $\beta V_{ext}(r)$ term. Finding an energy minimizing template can be as simple as using $\rho(r)$ to find F_{ex}, and finding the $\beta V_{ext}(r)$ expression which minimizes the grand canonical free energy.

Unsurprisingly, there are issues with this approach that must be addressed before designing new templates for directed self-assembly. As shown in Figure 6.5, when a free minimization is used to calculate the necessary external field for optimized square and

hexagonal structures, one obtains a high value for βV at each interstitial site of the target lattice. In order to generate templates in accordance with the pattern multiplication standards put forth in previous chapters of this dissertation, one must discover ways of parameterizing an external field in a way that favors sparse patterns. Furthermore, as the exact equilibrium density profile in the presence of an external field is unlikely to be a perfect 2D Gaussian curve (e.g. Figures 2.3, 2.4), it becomes a significant challenge to appropriately define the target profile used in the calculation of F_{ex}. One can imagine constructing an iterative computational algorithm which calculates a parameterized field in one step, then updates the FMT density profile within some quantitative constraints on peak height and standard deviation to preserve crystalline order. This process would then proceed until there is an equilibrium reached between a density profile that satisfies the requirements of a target structure and an optimized, sparse template geometry.

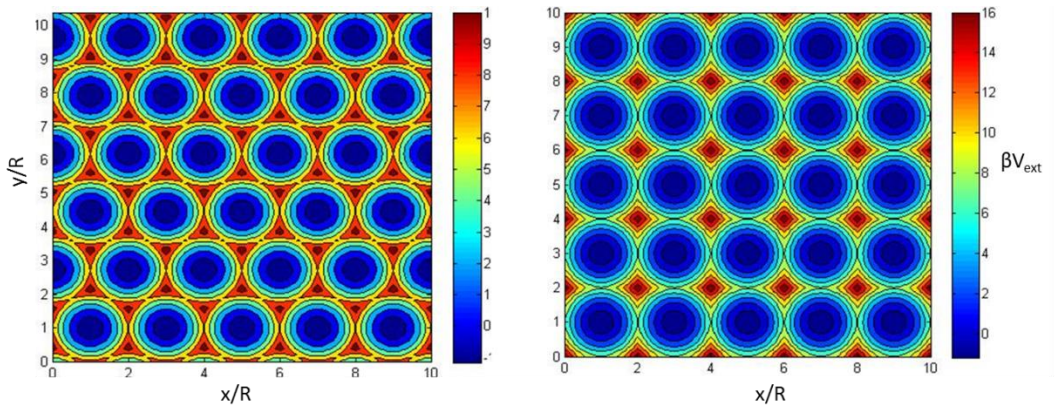

Figure 6.5: FMT generated energy minimizing fields for hexagonally close-packed (left) and square (right) 2D lattices. The density profile was constructed by Gaussian peaks at each lattice coordinate, which lie in the middle of the blue circular regions in the above plots. In each case, the calculated field is high in interstitial locations, even for the hcp structure which naturally forms in equilibrium with no field. This demonstrates that the calculated field can further stabilize naturally forming structures. However, since each interstitial site requires a template feature, there is no pattern multiplication from these fields. Further constraints must be applied to discover optimized sparse templates.

References

[1] H.A. Atwater and A. Polman, *Nature Materials* **9**, 205 (2010)

[2] A. Kuzyk, R. Schreiber, Z. Fan, G. Pardatscher, E-M. Roller, A. Hogele, F.C. Simmel, A.O. Govorov, and T. Liedl, *Nature* **483** 311 (2012)

[3] M. Albrecht, C.T. Rettner, A. Moser, M.E. Best, and B.D. Terris, *Appl. Phys. Lett*. **81**, 2875 (2002)

[4] H.J. Richter *et al*., *Appl. Phys. Lett*. **88**, 222512 (2006)

[5] J. An, Y-B. Kim, J. Park, T.M. Gur, and F.B. Prinz, *Nano Lett*. **13**, 4551 (2013)

[6] N. I. Zheludev, *Science* **328**, 582 (2010)

[7] N. I. Zheludev and Y. S. Kivshar, *Nature Materials* **11**, 917 (2012)

[8] V. M. Shalov, *Nature Photonics* **1**, 41 (2007)

[9] X. Chen, Y. Chen, M. Yan, and M. Qiu, *ACS Nano* **6**, 2550 (2012)

[10] A. V. Kabashin, P. Evans, S. Pastovsky, W. Hendren, G. A. Wurtz, R. Atkinson, R. Pollard, V. A. Podolskiy, and A. V. Zayats, *Nature Materials* **8**, 867 (2009)

[11] M. Malloy and L. C. Litt, *Journal of Micro/Nanolithograophy, MEMS, and MOEMS* **10**, 032001 (2011)

[12] X. Zhang, C. Sun, and N. Fang, *Journal of Nanoparticle Research* **6**, 125 (2004)

[13] D. Xin and B. A. Riggs, *Encyclopedia of Supramolecular Chemistry*, 120047104 (2012)

[14] G. M. Whitesides and B. Grzbowski, *Science* **295**, 2418 (2002)

[15] C. Knorowski, S. Burleigh, and A. Travesset, *Phys. Rev. Lett*. **106**, 215501 (2011)

[16] Y. Zhang, F. Lu, K.G. Yager, D. van der Lelie and O. Gang, *Nature Nanotechnology* **8**, 865 (2013)

[17] Q. Chen, S.C. Bae, and S. Granick, *Nature* **469**, 381 (2011)

[18] A. Reinhardt, F. Romano, and J. P. K. Doye, *Phys. Rev. Lett*. **110**, (2013)

[19] S. Sacanna, W. T. M. Irvine, P. M. Chaikin, and D. J. Pine, *Nature* **464**, 575 (2010)

[20] L. Filion, M. Hermes, R. Ni, E. C. M. Vermolen, A. Kuijk, C. G. Christova, J. C. P. Stiefelhagen, T. Vissers, A. van Blaaderen, and M. Dijkstra, *Phys. Rev. Lett.* **107**, 168302 (2011)

[21] P.F. Damasceno, M. Engel, and S.C. Glotzer, *Science* **337**, 453 (2012)

[22] A. Haji-Akbari, M. Engel, and S. C. Glotzer, *J. Chem. Phys.* **135**, 194101 (2011)

[23] C. Choi, K. Noh, Y. Oh, C. Kuru, D. Hong, D. Villwock, L-H. Chen, and S. Jin, *IEEE Transactions on Magnetics* **47**, 2536 (2011)

[24] N. V. Dziomkina and G. J. Vansco, *Soft Matter* **1**, 265 (2005)

[25] C.J. Duska and J.A. Floro, *J. Mater. Res.* **29**, 2240 (2014)

[26] C. Kocabas, S.-H Hur, A. Gaur, M.A. Meitl, M. Shim, J.A. Rogers, *Small* **1**, 1110 (2005)

[27] E. Winfree, F. Liu, L.A. Wenzler, and N.C. Seeman, *Nature* **394**, 539 (1998)

[28] S.M. Douglas, H. Dietz, T. Liedl, B. Hogberg, F. Graf, and W.M. Shih, *Nature* **459**, 414 (2009)

[29] N. R. Jana, *Angew. Chem. Int*. **43**, 1536 (2004)

[30] A.K. Boal, F. Ilhan, J.E. deRouchey, T. Thurn-Albrecht, T.P. Russell, and V.M. Rotello, *Nature* **404**, 746 (2000)

[31] P. Akcora et al., *Nature Materials* **8**, 354 (2009)

[32] A. Boker, J. He, T. Emrick, and T.P. Russell, *Soft Matter* **3**, 1231 (2007)

[33] P.F. Damasceno, M. Engel, and S.C. Glotzer, *ACS Nano* **6**, 609 (2012)

[34] Gronheid, R., & Nealey, P. (n.d.). Directed self-assembly of block co-polymers for nano-manufacturing: Processing, modeling, characterization and applications.

[35] R.A. Segalman, H. Yokoyama, and E. J. Kramer, *Adv. Mater*. **13**, 1152 (2001)

[36] R. A. Segalman, A. Hexemer, and E. J. Kramer, *Macromolecules* **36**, 6831 (2003)

[37] I. Bita, J.K.W. Yang, Y.S. Jung, C.A. Ross, E.L. Thomas, and K.K. Berggren, *Science* **15**, 939 (2008)

[38] J.Y. Cheng, C.T. Rettner, D.P. Sanders, H-C. Kim, and W.D. Hinsberg, *Adv. Mater.* **20**, 3155 (2008)

[39] E. Han, H. Kang, C.-C. Liu, P.F. Nealey, and P. Gopalan, Adv. Mater. **22**, 4325 (2010)

[40] Q. Tang, and Y. Ma, *Soft Matter* **6**, 4460 (2010)

[41] J. K. W. Yang, Y. S. Jung, J.-B. Chang, R. A. Mickiewicz, A. Alexander-Katz, C. A. Ross, and K. K. Berggren, *Nature Nanotechnology* **5**, 256 (2010)

[42] K. C. Daoulas, A. Cavallo, R. Shenhar, and M. Muller, *Phys. Rev. Lett*. **105**, 108301 (2010)

[43] X. Man, D. Andelman, and H. Orland, *Phys. Rev. E* **86**, 010801 (2012)

[44] J. Qin, G.S. Khaira, Y. Su, G.P. Garner, M. Miskin, H.M. Jaeger, and J.J. de Pablo, *Soft Matter* **9**, 11467 (2013)

[45] Z.h. Cai, K. Huang, P.A. Montano, T.P. Russell, J.M. Bai, G.W. Zajac, *J. Chem. Phys*. **98**, 2376 (1993)

[46] C.J. Hawker, E. Elce, J. Dao, W. Volksen, T.P. Russell, G.G. Barclay, Macromolecules, 29, 2686 (1996)

[47] E. Huang, T.P. Russell, C. Harrison, P.M. Chaikin, R.A. Register, C.J. Hawker, J. Mays, *Macromolecules* **31**, 7641 (1998)

[48] E. Huang, S. Pruzinsky, T.P. Russell, J. Mays, C.J. Hawker, *Macromolecules* **32**, 5299 (1999)

[49] M. Husseman, E.E. Malmström, M. McNamara, M. Mate, D. Mecerreyes, D.G. Benoit, J.L. Hedrick, P. Mansky, E. Huang, T.P. Russell, C.J. Hawker, *Macromolecules* **32**, 1424 (1999)

[50] P. Mansky, Y. Liu, E. Huang, T.P. Russell, C. Hawker, *Science* **275**, 1458 (1997)

[51] P. Mansky, T.P. Russell, C.J. Hawker, J. Mays, D.C. Cook, S.K. Satija, *Phys. Rev. Lett.* **79**, 237 (1997)

[52] T. Xu, C.J. Hawker, T.P. Russell, *Macromolecules* **38**, 2802 (2005)

[53] K. Almdal, J.H. Rosedale, F.S. Bates, G.D. Wignall, G.H. Fredrickson, *Phys. Rev. Lett*. **65**, 1112 (1990)

[54] F.S. Bates, *Science* **251**, 898 (1991)

[55] F.S. Bates and G.H. Fredrickson, *Annu. Rev. Phys. Chem*. **41**, 525 (1990)

[56] F.S. Bates, and G.H. Fredrickson, *Phys. Today* **52**, 32 (1999)

[57] M.J. Fasolka and A.M. Mayes, *Annu. Rev. Mater. Res.* **31**, 323 (2001)

[58] P.F. Green and R. Limary, *Adv. Colloid Interf. Sci*. **94**, 53 (2001)

[59] K.W. Guarini, C.T. Black, and S.H.I. Yeung, *Adv. Mater.* **14** (2002)

[60] M.W. Matsen and F.S. Bates *Macromolecules* **29** (1996)

[61] T.P. Russell, *Curr. Opin. Colloid Interface Sci*. **1**, 107 (1996)

[62] M.W. Geis, D.C. Flanders, and H.I. Smith, *Appl. Phys. Lett*. **35**, 71 (1979)

[63] J.Y. Cheng, C.A. Ross, E.L. Thomas, H.I. Smith, and G.J. Vansco, *Adv. Mater*. **15**, 1599 (2003)

[64] Y.S. Jung, W. Jung, and C.A. Ross, *Nano Lett*. **8**, 2975 (2008)

[65] M.J. Maher, C.T. Rettner, C.M. Bates, G. Blachut, M.C. Carlson, W.J. Durand, C.J. Ellison, D.P. Sanders, J.Y. Cheng, and C.G. Willson, *ACS Appl. Mater. Interfaces* **7**, 3323 (2015)

[66] R.A. Segalman, *Mat. Sci. Eng.* **48**, 191 (2005)

[67] J. Kao and T. Xu, *J. Am. Chem. Soc*. **137**, 6356 (2015)

[68] T. Hyeon, S.S. Lee, J. Park, Y. Chung, and H.B. Na, *J. Am. Chem. Soc*. **123**, 12798 (2001)

[69] P. Hu, L. Yu, A. Zuo, C. Guo, and F. Yuan, *J. Chem. Phys*, **113**, 900 (2009)

[70] E. Busseron, Y. Ruff, E. Moulin, and N. Giuseppone, *Nanoscale* **5**, 7098, (2013)

[71] S. Zhang, *Nature Biotechnology* **21**, 1171 (2003)

[72] K. Mangold, P. Leiderer, and Clemens Bechinger, *Phys. Rev. Lett.* **90**, 158302 (2003)

[73] A. van Blaaderen, M. Dijkstra, R. van Roij, A. Imhof, M. Kamp, B. W. Kwaadras, T. Vissers, and B. Liu, *Eur. Phys. J. Special Topics* **222**, 2895 (2013)

[74] A. C. Mitus, H. Weber, and D. Marx, *Phys. Rev. E* **55**, 6855 (1997).

[75] Y. Rosenfeld, *Phys. Rev. Lett.* **63**, 980 (1989)

[76] F-Q. You, Y-X. Yu, and G-H. Gao, *J. Phys. Chem. B* **109**, 3512 (2005).

[77] R. Roth, K. Mecke, and M. Oettel, *J. Chem. Phys.* **136**, 081101 (2012)

[78] M.P. Sears and L.J.D. Frink, *J. Comp. Phys.* **190**, 184 (2003)

[79] G. Doge, K. Mecke, J. Moller, D. Stoyan, R. P. Waagepetersen, *Int. J. Mod. Phys. C* **15**, 129 (2004)

[80] C. Tang, E. M. Lennon, G. H. Fredrickson, E. J. Kramer, C. J. Hawker, *Science* **322**, 429 (2008)

[81] B. Widom, *J. Chem. Phys.* **39**, 2808 (1963)

[82] M. C. Rechtsman, F. H. Stillinger, and S. Torquato, *Phys. Rev. Lett.* **95**, 228301 (2005)

[83] S. Torquato, *Soft Matter* **5**, 1157 (2009)

[84] A. V. Tkachenko, *Phys. Rev. Lett.* **106**, 255501 (2011)

[85] A. Jain, J. R. Errington, and T.M. Truskett, *Soft Matter* 9, 3866 (2013)

[86] M. C. Rechtsman, F. H. Stillinger, S. Torquato, *Phys. Rev. E* **73**, 011406 (2006)

[87] T.R. Albrecht et al., *IEEE Trans. Magn.* **49**, 773 (2013)

[88] A. Donev, J. Burton, F. H. Stillinger, and S. Torquato, *Phys. Rev. B* **73**, 054109 (2006)

[89] Y. Martinez-Raton, E. Velasco, and Luis Mederos, *J. Chem. Phys.* **125**, 014501 (2006)

[90] F.A. Escobedo and J.J. de Pablo, *J.Chem. Phys.* **105**, 4391 (1996)

[91] M. Gonzalez-Pinto, Y. Martinez-Raton, and E. Velasco, *Phys. Rev. E* **88**, 032506 (2013)

[92] M.E.Ferraro, R.T. Bonnecaze, and T.M. Truskett, *Phys. Rev. Lett*. **113**, 085503 (2014)

[93] S.A Jenekhe, X.L. Chen, *Science* **283**, 372 (1999)

[94] A. Tavakkoli K. G., K. W. Gotrik, A. F. Hannon, A. Alexander-Katz, C. A. Ross, K. K. Berggren, *Science* **336**, 1294 (2012)

[95] J. Gon Son, J.-B. Chang, K.K. Berggren, and C.A. Ross, *Nano Lett*. **11**, 5079 (2011)

[96] J.-B. Chang, J. Gon Son, A.F. Hannon, A. Alexander-Katz, C.A. Ross, and K.K. Berggren, *ACS Nano* **6**, 2071 (2012)

[97] K. Mangold, P. Leiderer, and C. Bechinger, *Phys. Rev. Lett*. **90**, 158302 (2002)

[98] M. Asbahi, K.T.P. Lim, F. Wang, H. Duan, N. Thiyagarajah, V. Ng, and J.K.W.Yang, *Langmuir* **28**, 16782 (2012)

[99] D. McDermott, J. Amelang, L.M. Lopatina, C.J. Olson Reichhardt, and C. Reichhardt, *Soft Matter* **9**, 4607 (2013)

[100] G. Doge, K. Mecke, J. Moller, D. Stoyan, and R.P. Waagepetersen, *Int. J. Mod. Phys. C* **15**, 129 (2004)

[101] W.G. Hoover, *J. Chem. Phys*. **57**, 1259 (1972)

[102] M.E. Ferraro, T.M. Truskett, and R.T. Bonnecaze, *Phys. Rev. E.*, **93**, 032606 (2016)

[103] Y. Tada, S. Akasaka, M. Takenaka, H. Yoshida, R. Ruiz, E. Dobisz, H. Hasegawa, *Polymer* **50**, 4250 (2009)

[104] G. Pandav, W.J. Durand, C.J. Ellison, C.G. Willson, and V. Ganesan, *Soft Matter* **11**, 9107 (2015)

[105] J.E. Lennard-Jones and A.F. Devonshire, *Proc. Roy. Soc.* **163A**, 53 (1937)

[106] W.G. Hoover and F.H. Ree, *J. Chem. Phys*. **49**, 3609 (1968)

[107] W.G. Hoover et al., *J. Chem. Phys.* **57**, 1259 (1972)

[108] X. Cottin and P. A. Monson, *J. Chem. Phys.* **99**, 8914 (1993)

[109] H.-L. Vortler, *Phys. Lett. A* **78**, 266 (1980)

[110] K. R. Hall, *J. Chem. Phys*. **57**, 2252 (1972)

[111] B. J. Alder, W. G. Hoover, and D. A. Young, *J. Chem. Phys.* **49**, 3688 (1968)

[112] H. Kuwamura, *Progress of Theoretical Physics* **61**, (1979)

[113] William G. Hoover, Nathan E. Hoover, and Kenton Hanson, *J. Chem. Phys.* **70**, 1837 (1979)

[114] R. J. Buehler, R. H. Wentorf, J. O. Hirschfelder and C. F. Curtiss, *J. Chem. Phys.* **19**, 61 (1951)

[115] K.W. Desmond and E.R. Weeks, *Phys. Rev. E* **80**, 051305 (2009)

[116] C. Fustin et al, *Langmuir* **20**, 9114 (2004)

[117] R. Tiruvalem et al., *J. Phys.: Conf. Series* **371**, 012028 (2012)

[118] A. Jain, J.R. Errington, and T. M. Truskett, *Soft Matter* **9**, 3866 (2013)

[119] A. Jain, Inverse Design Methods for Targeted Self-Assembly (2014) (Doctoral Dissertation)

[120] M. Torikai, *J. Chem. Phys.* **142**, 144102 (2015)